

SPARS ALGORITHMS AND SIMULATION RESULTS¹

D. C. Paulson, D. B. Jackson, and C. D. Brown
Aerospace Division
Honeywell Inc.
Minneapolis, Minnesota

ABSTRACT

This paper describes data processing algorithms for the LMSC/HI Space Precision Attitude Reference System (SPARS), emphasizing the application of discrete Kalman filter theory to the processing of data from the strapdown gyros and passive star sensors. The descriptions are at a level of detail that reflects refinement in digital simulation and real time system test. A three degree-of-freedom digital simulation, which includes the SPARS equations along with a "truth model" and dynamic error sources, is described. Results of simulation runs are presented which show sensitivity of attitude reference performance to star sensor geometry, measurement errors and detectability, to gyro drift and to computational errors. These results show that errors from the dynamic error sources are well within the SPARS requirements. Results of a series of simulation runs to determine convergence of the attitude error from large initial values (acquisition) are presented. Star sensor design parameters are shown to have a significant effect on convergence time. The paper concludes with a summary of computational requirements, showing that the SPARS algorithm can be implemented in a typical modern aerospace computer.

INTRODUCTION

The SPARS algorithms represent a new application of recursive filtering to strapdown sensor data for precise determination of satellite attitude. This paper presents a detailed description of these algorithms in the form they would be used in an orbiting vehicle with an on-board digital computer. An all-digital simulation, with which these algorithms have been analyzed and refined, is presented along with some simulation results. As described in more detail in Ref. 1, these results have been verified, using the SPARS algorithms in a slightly modified form, in a dynamic system laboratory test, which consisted of the real time determination of rate table attitude to high precision.

The coming of age of the high speed digital flight computer permits a transference of certain functions from the hardware to the software with

a consequent overall reduction in hardware complexity and improvement in system performance. In SPARS, the strapdown star sensors provide discretized, and the function of relating these to one another to bound the drift of the strapdown gyro data is performed in the computer. By providing near-instantaneous sensing of vehicle non-linear dynamics, the gyros create a reference trajectory about which attitude errors behave linearly, thus permitting use of linear recursive filtering without torque modeling. The recursive approach maintains a current and accurate attitude reference without the difficulties inherent in batch processing of large quantities of data.

The concept of applying recursive filtering to attitude determination was first proposed in the SPARS Phase O proposal in early 1967 (Ref. 2). In support of the proposal, a single degree-of-freedom simulation was performed. Simulation

¹The conception of the algorithms and the generation of the simulation program was Honeywell-sponsored in early 1967. The simulation analysis effort was carried out under subcontract 24-16582 to Lockheed Missiles and Space Company.

was expanded to a complete three degree-of-freedom simulation (described herein) in the mid-1967 period prior to commencement of the Phase O SPARS contract in December, 1967. The majority of the simulation effort was carried out under the Phase O contract (Ref. 3).

Most of the algorithm details, including the portions considered to be original, were developed in the mid-1967 time frame. The exception was the extension of the recursive approach to acquisition², an approach which was taken in Phase O after initial attempts to use a discrete batch processing approach had yielded poor results. Three noteworthy innovations devised for the SPARS application and incorporated into these algorithms are: 1) the particular use in the measurement calculation of the dot product between the star sensor detector slit normal and the star vector, 2) the use of the dot product variance, computed in the weighting function calculation, as a tolerance factor in the decision making process for star identification, and 3) the formulation of the noise term in the covariance matrix propagation using test-verified white noise drift.

These and the other SPARS algorithms, such as star catalog sorting, gyro rate calculation and integration, and derivations of the geometry matrix and transition matrix equations, are presented in a level of detail that is meant to convey the great depth to which algorithm development has progressed in the SPARS simulation and test program. The descriptions of the simulation program and simulation results are not presented in the same level of detail. The reader is referred to Ref. 3 for an in-depth treatment of these subjects.

SENSOR CONCEPT

The SPARS uses two complementing forms of sensor data; gyro data to provide an essentially continuous attitude reference, and star sensor data to bound the long term gyro drift. Strapped down mechanizations of both types of sensors are used. A brief description of these sensors follows; more detailed descriptions are given in Refs. 1 and 4.

The inertial reference assembly (IRA), described in Ref. 4, uses three single degree-of-freedom rate integrating gyros mounted with their input axes forming a nominally orthogonal triad. A ternary pulse rebalance mode is used to maintain good scale factor stability and minimize random drift. The IRA outputs are three asynchronous pulse trains, each pulse representing a fixed increment of the integral of rate experienced by the vehicle about the respective gyro input axis. Each pulse train is summed in a separate precounter, the contents of which are periodically strobed into a digital computer for solution of attitude change over the sample period.

²Suggested by Dr. J. L. Lemay

The relatively benign angular motion of the satellite enables this solution to be accomplished at a relatively low frequency without the usual concern for the "coning" considerations of strapdown attitude computations.

The two identical SPARS star sensors, also described in detail in Ref. 2, each utilizes medium field-of-view ($< 10^\circ$) concentric optics to image a portion of the celestial sphere on a detector surface. The detector consists of a number of photosensitive elements, hereinafter denoted as slits, arranged in a spoke-like array to take advantage of the relative motion of the star field caused by the nominal pitch motion of the Earth-stabilized vehicle. Fig. 1 shows the arrangement of the star sensor viewing directions and slit orientations with respect to the vehicle. The values of β and γ can be varied over a wide range to accommodate vehicle mounting constraints without significantly affecting attitude reference performance.

The basic star sensor measurement, referred to as a transit, is the epoch at which the image of a star crosses one of the photosensitive slits. This generates a current pulse which starts a counter that is terminated at the next IRA precounter sampling time. The contents of the star sensor counter are strobed into the digital computer along with the IRA data. These data allow correction of the attitude state at the precise instant that the transit occurred.

The orientations of the star sensor slits are precisely measured in a preflight calibration. A single transit provides information of vehicle orientation with respect to the measured star. Coupled with the knowledge of star celestial coordinates, a transit provides partial information of vehicle inertial attitude. Multiple transits on different stars and on slits of varying angle with respect to vehicle motion provide the necessary data for complete attitude update.

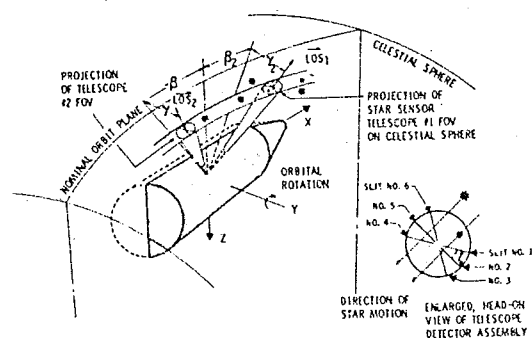


Fig. 1. Star Sensor-Vehicle Geometry

DATA PROCESSING CONCEPT

The SPARS data processing can be divided into two major categories: gyro data processing and star sensor data processing. These take place at different frequencies; the gyro data is processed at a constant frequency of several times per second, and the star sensor data is processed at irregular intervals as determined by star transits. Fig. 2 shows a block diagram with these functions further subdivided.

Gyro Data Processing

After processing in the precounters, the IRA gyro data is input to the computer for rate derivation, gyro bias compensation, gyro misalignment correction, and attitude (direction cosine) solution. Gyro data processing blocks are those in the lower half of Fig. 2.

Rate Derivation -- Let the sum of the gyro pulses be denoted by $\Delta\theta_i$ where $i = x, y, z$. These are measures of the integrals of rate about the respective gyro input axes over the sampling interval. A first order approximation for rate would yield $\omega_{gi} = \Delta\theta_i / \Delta t$ and the so-called commutation error, which arises from the fact that angles are not vectors and thus do not commute.

The commutation error occurs only when there are simultaneous rates about two or more axes. The magnitude of a typical error term per sample is roughly given by the product of the accumulated angle integrals (in radians) about two input axes over a sampling interval. For nominal body rates and sampling intervals in the SPARS application, the commutation error will introduce an equivalent drift into the body attitude solution that is less than one tenth the random gyro drift. However, for worst case body rates, the drift becomes sufficiently large such that a correction is desirable.

A straightforward method of correction is provided by fitting a polynomial to successive values of a $\Delta\theta_i$, then differentiating that function to obtain rate at the end points. This approach has been taken, using a second order curve fit (Ref. 5). An equivalent result was obtained in Ref. 6. The expression resulting for derived gyro rate $\bar{\omega}_g$ is (from Ref. 5):

$$\omega_{E_i}(i_k) = [\Delta\theta_i(t_k) - \Delta\theta_i(t_{k-1})] \frac{1}{2\Delta t} \quad (1)$$

where $\Delta\theta_i(t_k)$ is the precounter sum over the last sampling interval, Δt , for the i th gyro ($i = x, y, \text{ or } z$) and $\Delta\theta_i(t_{k-1})$ is the sum over the

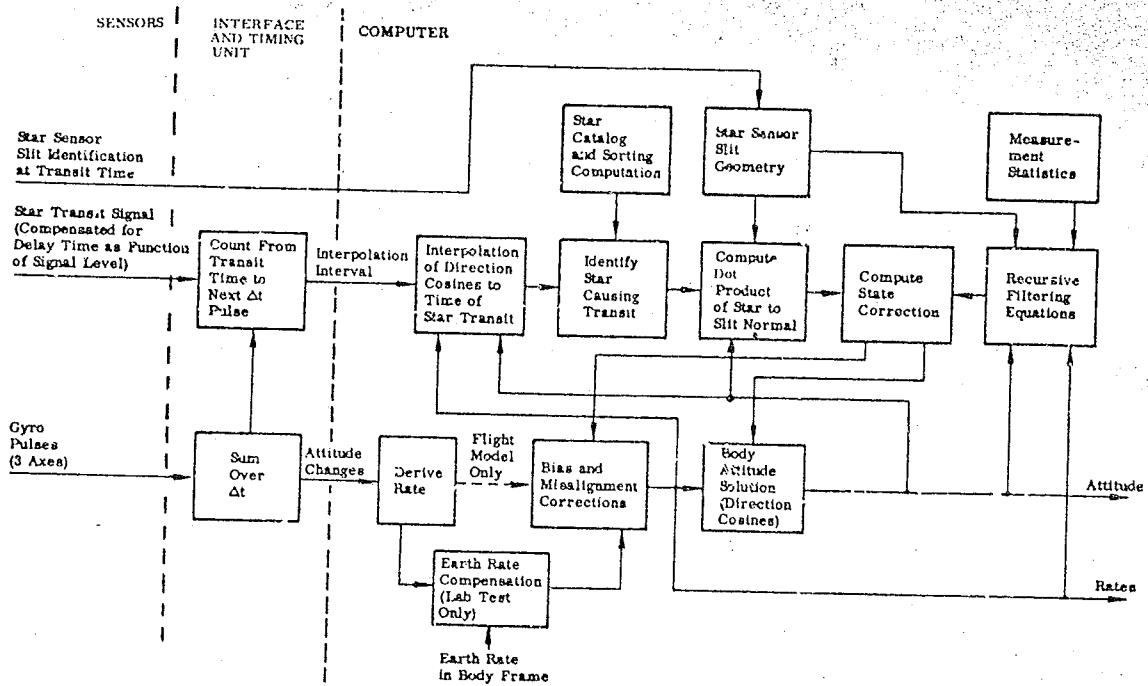


Fig. 2. Block Diagram of SPARS Computational Function

previous sampling interval for that same gyro. Equation (1) yields a second-order estimate of the gyro sensed rates at the end of the most recent sampling interval (t_k).

Rates at the beginning of that interval are given by

$$\omega_{g_i}(t_{k-1}) = [\Delta\theta_i(t_k) + \Delta\theta_i(t_{k-1})] \frac{1}{2\Delta t} \quad (2)$$

Both $\omega_{g_i}(t_k)$ and $\omega_{g_i}(t_{k-1})$ are used in the body attitude solution described in a later paragraph. Only $\omega_{g_i}(t_k)$ is used for the rate output.

Gyro Non-orthogonality Correction -- The actual alignments of the gyro input axes are not critical, but must be measured and compensated for accurately. The equation for the compensation is:

$$\bar{\omega}_o(t_k) = [T_{on}] \bar{\omega}_g(t_k) \quad (3)$$

and

$$\bar{\omega}_o(t_{k-1}) = [T_{on}] \bar{\omega}_g(t_{k-1})$$

where

$$\bar{\omega}_g(t) = \begin{bmatrix} \omega_{gx}(t) \\ \omega_{gy}(t) \\ \omega_{gz}(t) \end{bmatrix}$$

and

$$[T_{on}] \text{ is a } 3 \times 3 \text{ matrix,}$$

generally non-orthogonal, which is determined in a pre-flight calibration of the IRA. The resultant orthogonal rate vectors $\bar{\omega}_o(t_k)$ and $\bar{\omega}_o(t_{k-1})$ represent the measured rate components along the same three axes to which the star sensor photosensitive elements are referenced.

Gyro Drift Compensation -- Estimated vehicle rates, $\bar{\omega}$, are obtained by adding the gyro drift compensation vector, \bar{B}_g , to the orthogonal measured rates

$$\bar{\omega}(t_k) = \bar{\omega}_o(t_k) + \bar{B}_g \quad (4)$$

and

$$\bar{\omega}(t_{k-1}) = \bar{\omega}_o(t_{k-1}) + \bar{B}_g \quad (5)$$

which implies that the components of \bar{B}_g are correction terms for drift about the orthogonal body reference axes rather than the gyro input axes. Since these corrections are for constant drift, there is no need to apply the compensation about the gyro input axes. Furthermore, the elements of \bar{B}_g are updated periodically from star sights, which are all related to the orthogonal body reference axes. Use of gyro drift corrections in these same axes saves one extra coordinate transformation. The updating of \bar{B}_g is described in a later paragraph.

Body Attitude Solution -- There are many types of parameters which can be used to implement the numerical solutions of attitude from

gyro-measured rates. Among these are Euler angles, direction cosines and symmetrical Euler parameters (a form of quaternions). Euler angles are undesirable in that a numerical solution of equations using them involves time-consuming trigonometric functions. Direction cosines involve only multiplications and additions in the solution, but there are nine equations which must be solved. Symmetrical Euler parameters hold some advantages in that there are only four equations to be solved, again involving only multiplications and additions. However, since the attitude output of SPARS is to be used in coordinate transformations for Earth targeting, direction cosines will be necessary in any case. This would require a special transformation from the four-parameter set to direction cosines, taking extra computer storage as well as computation time. Therefore, direction cosines have been chosen for the SPARS body attitude solution.

The equations to be solved are:

$$\lambda_n(t_k) = \lambda_n(t_{k-1}) + \int_{t_{k-1}}^{t_k} [\omega_z \mu_n - \omega_y \nu_n] dt$$

$$\mu_n(t_k) = \mu_n(t_{k-1}) + \int_{t_{k-1}}^{t_k} [\omega_x \nu_n - \omega_z \lambda_n] dt \quad (6)$$

$$\nu_n(t_k) = \nu_n(t_{k-1}) + \int_{t_{k-1}}^{t_k} [\omega_y \lambda_n - \omega_x \mu_n] dt$$

where λ_n , μ_n , ν_n denote direction cosines between the body x, y, z axes, respectively, and the nth inertial axis ($n = 1, 2, 3$). The times t_k and t_{k-1} denote present and last previous times at which the gyro precounters were sampled.

Equations (6) are solved numerically by a second order improved Euler integration scheme. The rates $\omega(t_{k-1})$ and $\omega(t_k)$ from Eqs. (4) and (5) represent the rates at the beginning and the end of the integration interval, and are substituted into Eq. (6) for the ω_i ($i = x, y, z$) as appropriate for the second order solution.

The body attitude solution is incremental in nature rather than absolute, and as such the gyro precounters must be sampled and processed without losing any data. This implies use of an interrupt in interfacing the gyro precounters with the computer.

The nine direction cosines of Eqs. (6) receive their initial conditions from and are updated periodically by the star sights, which bound the errors in attitude resulting from random gyro drift and other lesser error sources. Among these lesser error sources are the effects of computational roundoff and truncation as well as the commutativity effect mentioned earlier. The computational errors will cause the direction cosines (hereinafter denoted collectively as T_{BI}) the 3 x 3 transformation from inertial to body

coordinates) to become non-orthogonal. This is corrected as part of the attitude updating process once per star sight, as described in a later paragraph. The overall effects of computational errors are described in a later portion of this paper.

Star Sensor Data Processing

The processing of data from the star sensor is shown in the upper half of Fig. 2. Based on the input star sensor counter value, the attitude matrix is interpolated back to the star transit time, the star involved in the transit is identified, a dot product is computed using aberration corrected star catalog data, and the attitude and gyro bias states are corrected using a Kalman filter-generated weighting function.

Interpretation of Star Sensor Input Data -- As described earlier, a star sensor transit pulse starts a counter in the interface and timing unit which is terminated at the next gyro sampling instant. The contents of the counter, termed the interpolation interval, is input to the computer along with the gyro data. Also input to the computer at the same time is a coded word indicating which slit was involved in the transit. This latter information is not actually necessary during steady state operation when the attitude uncertainty is sufficiently small to permit slit identification in the software. However, information is necessary for the acquisition process from large initial attitude uncertainties, as will be explained later.

The interpolation interval is added to the star sensor time delay, which is predetermined from a star sensor calibration, and the sum is used to define the limits in Eqs. (6) for an integration of the attitude matrix backward from t_k to the time of transit. Note that this calculation is performed only when a transit has occurred within the last gyro sampling interval, which is seldom, relative to frequency of solutions of Eqs. (6).

Star Catalog and Sorting Computation -- Before the attitude matrix at transit time can be used to compute the star measurement, the star involved in the transit must be identified.

The on-board star catalog consists of the right ascension, α_c , and declination, δ_c , in fixed inertial coordinates, of all stars to be utilized in a given mission. It is conceivable that this catalog could include only a segment of the celestial sphere covering a "swath" equal to the sensor field of view plus allowances for limit cycle excursions and orbital precession. However, this implies prior knowledge of the orbit orientation in inertial space, which could be changed considerably due to launch delays.

Rather than require changes in the star catalog right up to the time of launch, it is considered desirable to pay the small penalty in computer storage necessary to store coordinates of all detectable stars in the celestial sphere.

For convenience in sorting, a special, temporary star catalog is periodically created in the computer from the inertial catalog described above. It is an orbit-oriented catalog, for which right ascension, α^o , and declination, δ^o , with respect to a nominal orbit plane, are computed for each star. The computation uses a transformation, T_{OI} , relating orbital to inertial coordinates. It is defined as

$$T_{OI} = \begin{bmatrix} -\cos i_o \sin \Omega_o & \cos i_o \cos \Omega_o & \sin i_o \\ -\sin i_o \sin \Omega_o & \sin i_o \cos \Omega_o & -\cos i_o \\ -\cos \Omega_o & -\sin \Omega_o & 0 \end{bmatrix} \quad (7)$$

where i_o and Ω_o are the nominal orbit inclination and nodal longitude, respectively. The equations for α^o and δ^o are:

$$\alpha_o = \arctan(\mu_s^o / \lambda_s^o) \quad (8)$$

and

$$\delta_o = \arctan \frac{v_s^o}{\sqrt{1 - (v_s^o)^2}} \quad (9)$$

where

$$\begin{bmatrix} \lambda_s^o \\ \mu_s^o \\ v_s^o \end{bmatrix} = [T_{OI}] \begin{bmatrix} \cos \alpha_c \cos \delta_c \\ \sin \alpha_c \cos \delta_c \\ \sin \delta_c \end{bmatrix} \quad (10)$$

Only those stars which are within a certain range of declinations are put in the temporary catalog. The range of declinations is defined by the sensor field of view plus an allowance for limit cycle excursions. Those within the range form a "swath" of stars for which only the right ascension and an identification number (referring to the permanent inertial catalog) are stored. A schematic of a swath in a portion of the celestial sphere is shown in Fig. 3. Only one such swath is needed if the two star sensor telescopes are mounted on the same side of the vehicle at the same angle from the orbital plane. The swath must be updated periodically to account for orbital precession.

In addition to the above once per day sorting on declination, the number of candidate stars can be further reduced at the time of transit by sorting on right ascension. This is done by computing the right ascensions, α_{s1} , and α_{s2} , of both star sensor telescope optical axes in the orbit coordinate frame, then retaining for star identification, only those stars whose α^o are within a range of one of these two values (see Fig. 3). The sensor right ascensions in the orbit frame are:

$$\alpha_{s1} = \arctan(v^o_{LOS1} / \mu^o_{LOS1}) \quad (11)$$

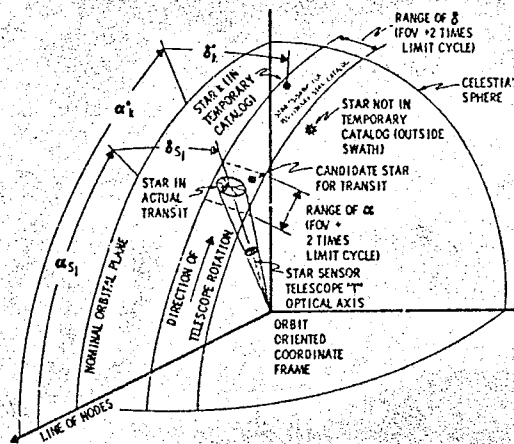


Fig. 3. Star-Telescope-Swath Geometry

$$\alpha_{s2} = \arctan \left(\frac{\lambda^{\circ} \text{LOS}_2}{\mu^{\circ} \text{LOS}_2} \right) \quad (12)$$

where

$$\begin{bmatrix} \lambda^{\circ} \text{LOS}_l \\ \mu^{\circ} \text{LOS}_l \\ \nu^{\circ} \text{LOS}_l \end{bmatrix} = \begin{bmatrix} T_{OI} \\ T_{BI}(t_m) \end{bmatrix}^T \text{LOS}_l^B \quad (l=1, 2) \quad (13)$$

and where LOS_1^B and LOS_2^B are the two vectors defining the star sensor telescope optical axes in the body reference frame; these are stored constants. The transformation, $T_{BI}(t_m)$, is the body attitude solution interpolated back to the time of measured transit.

Equations (11) and (12) are used, together with the temporary star catalog (stored in order of increasing α° to simplify sorting), to determine those stars which are within the candidate range for transit. Each such star is corrected for aberration and used in a final star identification.

Aberration Correction -- Correction for aberration of the apparent star positions must be made for both vehicle velocity around the Earth and Earth velocity around the Sun. The corrections are necessary because the effect of

these velocities causes shifts in apparent star position by several seconds of arc over an orbit and/or mission.

Only rough estimates of vehicle and Earth velocity are needed to make adequate aberration corrections. To obtain the components of Earth velocity around the Sun, the value of time, t , and initial Earth angle in the Ecliptic, ϕ_E , (for $t = 0$) are required. Earth velocity is then roughly

$$\vec{V}_E = v_{E \text{ avg}} \begin{bmatrix} \cos \left(\frac{2\pi}{8760} t + \phi_E \right) \\ (\cos i_E) \sin \left(\frac{2\pi}{8760} t + \phi_E \right) \\ (\sin i_E) \sin \left(\frac{2\pi}{8760} t + \phi_E \right) \end{bmatrix} \quad (14)$$

where $v_{E \text{ avg}}$ is the average linear velocity of the Earth around the Sun, i_E is the inclination of the elliptic to the equator, and t is in hours.

The vehicle velocity, \vec{V}_S , may be provided from an external computation to SPARS, or it may be estimated from body attitude as follows:

$$\vec{V}_S = \begin{bmatrix} X_B^I \end{bmatrix} \vec{V}_{S \text{ avg}} \quad (15)$$

where $\vec{V}_{S \text{ avg}}$ is an average linear velocity of the vehicle around the Earth and X_B^I is the transpose of the first row in the body attitude matrix, T_{BI} ; i.e., λ_1, λ_2 , and λ_3 from Eqs. (6). Equation (15) is valid when the vehicle is Earth-stabilized in a near-circular orbit.

The aberration correction for both the above velocities is a simple vector addition

$$\vec{S}_k^I = \frac{\vec{V}_E + \vec{V}_S}{c} + \begin{bmatrix} \cos \alpha_{ck} \cos \delta_{ck} \\ \sin \alpha_{ck} \cos \delta_{ck} \\ \sin \delta_{ck} \end{bmatrix} \quad (16)$$

where \vec{S}_k^I is the apparent position of the k^{th} star in the Cartesian inertial frame, c is the speed of light, and the terms in the brackets are the vector components of the k^{th} star in inertial coordinates as calculated from the stored right ascension α_{ck} and declination δ_{ck} . The result from Eq. (16) is not a unit vector; however, the deviation is so small (on the order of one part in 10^5) that normalization of \vec{S}_k^I is not necessary.

For each star that is identified as a transit candidate using the temporary, orbit oriented star catalog, the correction of Eq. (16) is made prior to final star identification. The identification number stored in the temporary catalog provides the means for referring back to the inertial α_c and δ_c for use in Eq. (16).

Dot Product Computation and Star Identification -- The parameter used in final

identification of the star involved in the transit is the value of the star sensor measurement; i.e., the dot product between the star vector and the star sensor detector slit normal.

For a transit to occur, a star vector must intersect one of the star sensor photodetector slits. As shown in Fig. 4, the photodetectors in either telescope consist of six slits across the field of view. It is assumed that each detector slit defines a single plane with the telescope optical axis. The j^{th} slit plane is defined by a unit normal vector, \bar{I}_{N_j} . Deviations along any slit from the planar assumption represents one of the error sources in star measurements. Part of this error can be removed with appropriate calibration and software.³

When a star vector intersects a slit plane, the dot product of the star vector and the normal to that plane should be zero. That is, $\text{DOT} = 0$ in

$$\text{DOT} = \bar{I}_{N_j} \cdot \bar{S}_k \quad (17)$$

for the correct star, k .

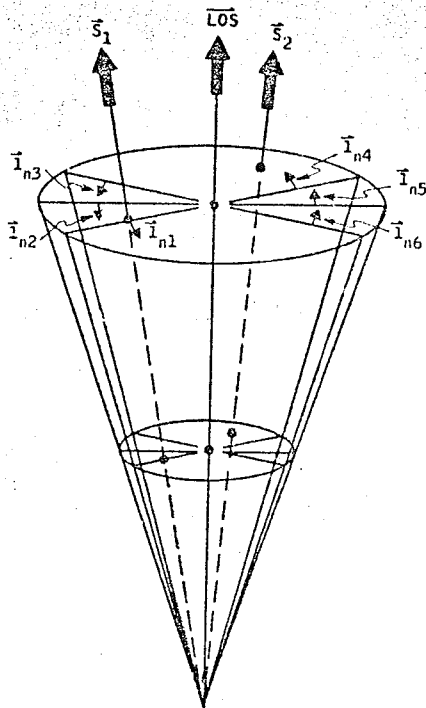


Fig. 4. Star-Telescope Geometry at Time of Transit

³Six slits are used in SPARS. A larger number of slits may be used with a correspondingly larger number of defining vectors.

The slit normal vector, \bar{I}_{N_j} , is fixed in body coordinates, whereas the star vector, \bar{S}_k , is fixed (except for aberration corrections) in inertial coordinates. In order to evaluate DOT, one of these vectors must be transformed into the frame of the other. The transformation involved is that resulting from the body attitude solution, T_{BI} . If we choose to resolve the star vector into body coordinates, Eq. (17) can be written as:

$$\text{DOT} = \bar{I}_{N_j}^B \cdot \left\{ \left[T_{BI}(t_m) \right] \bar{S}_k^I \right\} \quad (18)$$

where the t_m indicates that the specially evaluated T_{BI} at the transit time is used in the solutions of Eq. 18.

The procedure for finding the star causing the transit is to evaluate DOT for each candidate, using the \bar{I}_{N_j} for the slit identified by the input identification word, and compare the result with a preset threshold or tolerance. The latter is a function of the system performance level, determined by the Kalman filtering calculations, and is described in a later paragraph. DOT for the correct star should be less than the tolerance; all other DOTs should be larger.

If more than one of the star candidates yield a $|\text{DOT}|$ less than the tolerance (which is extremely unlikely during steady state operation when the tolerance level is very small), the measurement is declared invalid and no state corrections are made. Similarly, if none of the candidates yield a $|\text{DOT}|$ less than the tolerance (as would be the case when a star that is not in the catalog has caused the transit), the measurement is disregarded. This technique eliminates the probability that uncatalogued stars, illuminated dust particles, or ambiguous transits can cause improper state corrections to be made. Furthermore, it enables exercise of choice in selecting the on-board star catalog, in that all detectable stars need not be catalogued. In regions of the sky where stars are more closely spaced, only selected stars would be catalogued, which reduces computer storage without sacrificing overall system performance.

When a single valid transit candidate has been identified, the value of DOT for that star is used for the state correction. Note that for a perfect star sensor measurement DOT represents the sine of the angle which is the projection of the system attitude error onto a plane parallel to the star vector and perpendicular to the slit plane. Since DOT is small at a transit calculation, a first order approximation can be made equating DOT to the value of the above error angle in radians. This is the quantity to be multiplied by the Kalman weighting vector for state correction.

State Correction -- The SPARS data processing concept makes use of linear recursive filtering theory to correct state. Since the basic SPARS equations of attitude are non-linear, they must be linearized to apply this theory. The

approach is valid if the system behaves linearly when perturbed about the non-linear solution, obtained numerically in the on-board computer. This is true in the SPARS case.

Although the non-linear solution of attitude utilizes direction cosines, it is undesirable to linearize these equations to define state. They are nine parameters, and are not independent. Instead, three independent Euler angles are used, along with the three gyro bias correction terms, as the variables from which linearized state is derived. The state, X , is defined as

$$\bar{X} = \begin{bmatrix} \delta \phi \\ \delta \theta \\ \delta \psi \\ \delta B_x \\ \delta B_y \\ \delta B_z \end{bmatrix} \quad (19)$$

where the top three elements are linearized Euler angles and the bottom three are linearized gyro bias corrections. The incremental correction to state is given by

$$\Delta \bar{X} = \bar{K} \cdot (\text{DOT}) \quad (20)$$

where \bar{K} is a six-element weighting vector, the generation of which is described in a later paragraph.

In order to apply this state correction after a star transit, the direction cosines of the body attitude solution must first be converted to Euler angles. The corrections of Eq. (20) are then added, the first three elements of $\Delta \bar{X}$ to the Euler angles, and the last three to the gyro bias correction terms B_x , B_y , and B_z [used in Eqs. (4) and (5)]. Although this conversion to and from Euler angles would seem to require extra computation time as well as storage relative to performing all computations with Euler angles, overall time is actually reduced because the high speed body attitude solution utilizes direction cosines, which are more efficient, as discussed in a previous paragraph. Furthermore, the procedure automatically orthogonalizes the direction cosine matrix, thus no special function is needed for this purpose.

The equations used to perform the transformations between direction cosines and Euler angles depend on the Euler angle sequence. To avoid singularities involved in computing Euler angles from direction cosines, the sequence is defined relative to the orbit-oriented coordinate frame. Use of a pitch-roll-yaw (θ - ϕ - ψ) sequence then avoids the "gimbal lock" problem in that the roll and yaw angles are known to not exceed a few degrees.

The Euler angles for this sequence are related to the direction cosines by

$$T_{BI}(t) = \begin{bmatrix} \cos\phi \cos\theta & \sin\phi \cos\theta & -\sin\theta \\ \sin\phi \cos\theta & \cos\phi \cos\theta & \sin\theta \\ \cos\phi \sin\theta & \sin\phi \sin\theta & \cos\theta \end{bmatrix} [T_{OI}] \quad (21)$$

where $[T_{OI}]$ is the inertial-to-orbit transformation defined by Eq. (7) once per day. From this are defined the Euler angles

$$\phi = \arctan \frac{-v_2^0}{\sqrt{1-(v_2^0)^2}} \quad (22)$$

$$\theta = \arctan \left(v_1^0 / v_3^0 \right)$$

$$\psi = \arctan \left(\lambda_2^0 / \mu_2^0 \right)$$

where λ_2^0 , μ_2^0 , v_1^0 , v_2^0 , and v_3^0 are elements of

$$\left[T_{BO}(t) \right] = \left[T_{BI}(t) \right] \left[T_{OI} \right]^T \quad (23)$$

The computational functions of star catalog sorting, aberration correction, and transit time prediction may take as long as one or two gyro precounter sampling intervals to complete. It is assumed that the linear correction to state can be made at that time rather than at the time of measurement with negligible error. The last solution of $T_{BI}(t_k)$ is thus used in Eqs. (23) and (22) to compute Euler angles. After the corrections to state are applied by adding the elements of $\Delta \bar{X}$ from Eq. (20) to the appropriate Euler angles and gyro bias compensation terms, the conversion back to direction cosines is made, using Eq. (21), to obtain the updated attitude at the same time, t_k . This becomes the new initial condition for the body attitude solution, Eq. (6).

Weighting Function Generation -- As described in the preceding section, the SPARS data processing concept is an application of linear recursive estimation theory. This theory is well known and documented in the literature; Ref. 7 gives an over-all view with pertinent comments that will be referenced herein.

The essence of linear estimation theory is the solution of a (six element) weighting vector, K , which provides a means for correcting state in real time that minimizes the expectation of error in a least squares sense. The weighting function is computed from a 6 x 6 covariance matrix, P , which is a running estimate of system error statistics. As derived in Ref. 7, the computation is

$$\bar{K} = PH^T [HPH^T + R]^{-1} \quad (24)$$

where H is a geometry matrix of partial derivatives relating perturbations in state to perturbations in measurement, and R is the estimated measurement covariance matrix. For the SPARS case, the measurement is a scalar, hence R is the variance of the star sensor uncertainty in angular units. Eq. (24) is solved once per star transit and used in the state correction. The geometry matrix (a 1 x 6 row vector in this case), is derived in Appendix A to be:

$$H = H \begin{pmatrix} \bar{1}_{N_j}^B & T_{BI} & T_{OI} & \bar{S}_k^I \end{pmatrix} \quad (25)$$

The covariance matrix, P, in Eq. (24) is time variant. In the SPARS application, its computation can be discrete (see Ref. 7) since the star measurements occur relatively infrequently with respect to the high speed solution of state. In the discrete computation, the covariance matrix, P, is propagated from the time of one measurement to the next by means of a 6 x 6 transition matrix, $\Phi(t_k; t_{k-1})$, which is defined as that matrix which relates linearized state, \bar{x} , from one time, t_{k-1} , to the next, t_k , by

$$\bar{x}(t_k) = \left[\Phi(t_k; t_{k-1}) \right] \bar{x}(t_{k-1}) \quad (26)$$

The propagation equation is:

$$P(t_k) = \Phi(t_k; t_{k-1}) P(t_{k-1}) \Phi^T(t_k; t_{k-1}) + U(t_k) \quad (27)$$

where t_{k-1} and t_k are times of the previous and present star transits, respectively, and $U(t_k)$ is a matrix representing the contributions to system errors, between measurements, of unmodeled or inaccurately modeled system dynamics, i.e., plant noise. Included in the latter are computational errors, and most importantly, random gyro drifts.

The transition matrix, $\Phi(t_k; t_{k-1})$, is obtained by numerical integration of the equation

$$\frac{d}{dt} \left[\Phi(t; t_{k-1}) \right] = [F(t)] \left[\Phi(t; t_{k-1}) \right] \quad (28)$$

Since [F] is a matrix of time varying coefficients from the body attitude solution, this integration must take place in parallel with the solution of Eq. (6). The matrix [F] is derived in Appendix B, and is as follows:

$$F(t) = \begin{bmatrix} 0 & 0 & -p \sin \psi + q \cos \psi & \cos \psi & -r \sin \psi & 0 \\ (p \sin \psi + q \cos \psi) \frac{\sin \psi}{\cos \psi} & 0 & p \cos \psi - q \sin \psi & \frac{\sin \psi}{\cos \psi} & \frac{\cos \psi}{\cos \psi} & 0 \\ (q \cos \psi + p \sin \psi) \frac{\sin \psi}{\cos \psi} & 0 & (p \cos \psi - q \sin \psi) \tan \psi & \sin \psi \tan \psi & \cos \psi \tan \psi & 1 \\ 0 & 0 & 0 & 0 & 0 & 0 \\ 0 & 0 & 0 & 0 & 0 & 0 \\ 0 & 0 & 0 & 0 & 0 & 0 \end{bmatrix} \quad (29)$$

⁴ v_1^2 , v_2^2 , and v_3^2 are in units of (drift)²/Hz.

where $p = \omega_x$, $q = \omega_y$, $r = \omega_z$, and ϕ , θ , ψ are the Euler angles relating body attitude to the orbital coordinate frame. The initial condition to Eq. (29) is $\Phi(t_{k-1}; t_{k-1}) = I$ (unity matrix). A rectangular integration algorithm for solution of Eq. (28) is adequate, since precision is not critical. The elements $\sin \psi$, $\sin \phi$, $\cos \psi$, etc. in F(t) can be derived from the attitude matrix $T_{BI}(t)$ [see Eq. (21)] by simple arithmetic operations without inverse trigonometric functions.

At the time of a valid transit, Eqs. (27), (25), and (24) are solved in that order. The weighting vector, K, is used to apply a state correction according to Eq. (20). The additional equation

$$P = P - KHP \quad (30)$$

must also be solved to update the covariance matrix for error improvement resulting from the state correction. The result of this calculation is stored for propagation ahead by Eq. (27) at the time of the next transit.

Determination of the "Noise Matrix," U(t)

The matrix U(t_k) in Eq. (27) must be somewhat empirical inasmuch as it accounts for both known (statistically) and unknown plant noise. However, if the assumption is made that the unknown plant noise is small compared to the known, then an approximate form for U(t_k) can be derived. In this case, random gyro drift is the dominant known plant noise. Assuming this to be a white noise process (evidence of this from test data is given in a later paragraph) the form of U is derived in Appendix C to be:

$$U(t_k) = \begin{bmatrix} v_1^2 \Delta t_T & 0 & 0 & 0 & 0 & 0 \\ 0 & v_2^2 \Delta t_T & 0 & 0 & 0 & 0 \\ 0 & 0 & v_3^2 \Delta t_T & 0 & 0 & 0 \\ 0 & 0 & 0 & 0 & 0 & 0 \\ 0 & 0 & 0 & 0 & 0 & 0 \\ 0 & 0 & 0 & 0 & 0 & 0 \end{bmatrix} \quad (31)$$

where v_1^2 , v_2^2 , v_3^2 are the components of low frequency gyro drift power spectral density⁴, and Δt_T is the time since the last transit. This form is approximate in that the assumptions of constant pitch rate and zero roll and yaw rates are necessary to obtain a solution. The exact representation of the effect of white noise gyro drift could be handled by solving the linear symmetric matrix differential equation

$$\frac{d}{dt} [P(t)] = F(t) P(t) + P(t) F^T(t) + Q(t) \quad (32)$$

in place of Eqs. (27) and (28), where Q(t) is the expected covariance of the noise $\bar{v}(t)$ in the standard equation

$$\frac{d}{dt} [\bar{x}(t)] = F(t) \bar{x}(t) + \bar{v}(t) \quad (33)$$

That is,

$$E [\vec{v}(t) v^T(\tau)] = Q(t) \delta(t-\tau) \quad (34)$$

for white noise, where δ is the Dirac delta function.

This approach is not taken in SPARS, primarily because the solution of Eq. (32) is slightly more complex than solving Eqs. (27) and (28), and the performance obtained with the latter is satisfactory.

Equation (31) must be augmented in practical application to account for the unknown plant noise (e.g., computational errors). Experience in the SPARS application has shown that use of the other three diagonal terms is sufficient. These are determined by empirical means. Constant and time dependent terms have been tried with approximately equivalent results.

SIMULATION AND MODELING

The complexity and non-linearities of the SPARS problem necessitated the use of digital simulation techniques for performance studies. Interrelationship of error sources required the use of a single, comprehensive digital simulation. As shown in Fig. 5, the simulation consists of two main parts; a truth model, which simulates vehicle and sensor dynamics, and the SPARS algorithms. The latter are essentially those equations and logic discussed in the previous sections and need no further explanation. The remainder of this section describes the truth model, i.e. the left-hand side of Fig. 5, and the error processing techniques.

The major elements of the truth model are the star transit calculations, the attitude and limit cycle solutions, and the sensor error models.

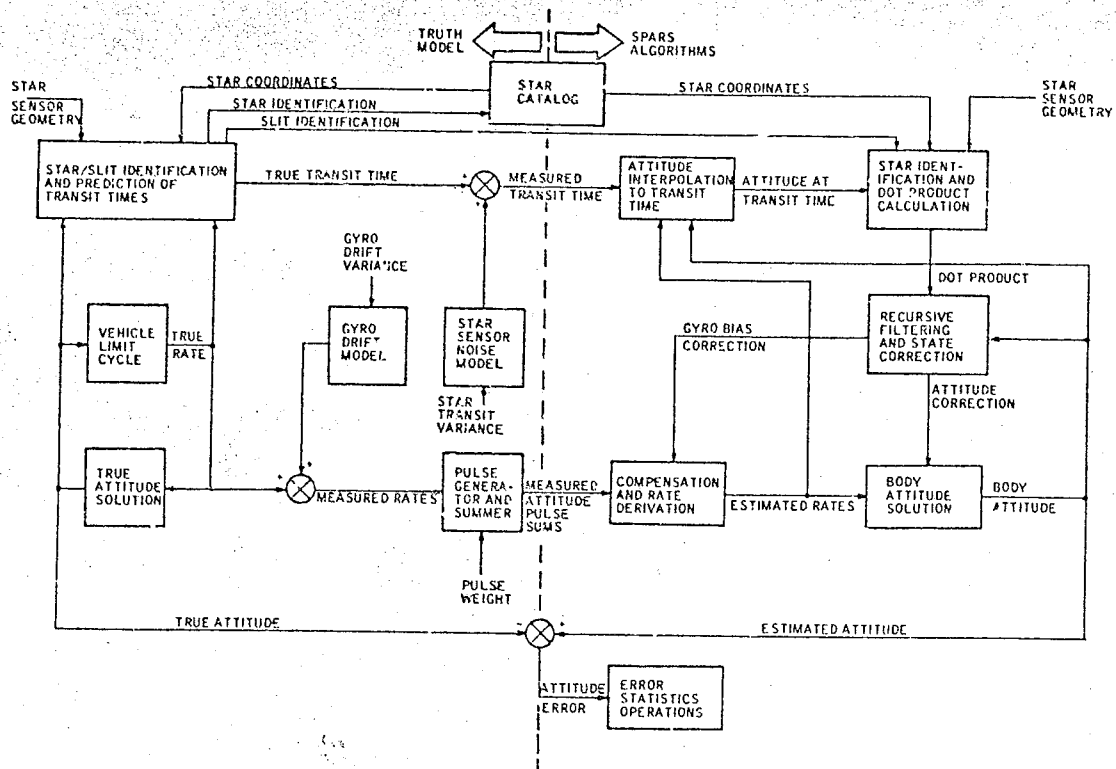


Fig. 5. Three-Degree-of-Freedom SPARS Simulation Block Diagram

Star Transit Calculations

A star transit prediction table is maintained in the truth model for generation of true transit times. Each time one of the imaginary leading edges (which are a fixed angular distance ahead of the star sensors as shown in Fig. 6) passes a star, a linear prediction of transit time is computed, using true rates and attitudes, and entered into the table. When the predicted transit time is within 150 seconds of computed current time, the transit is re-predicted and the table is updated. This is repeated 15 seconds before estimated transit and for every Δt thereafter until the transit occurs or until the sensor passes by the star. Attitude is interpolated within the last Δt using a Newton-Raphson iteration on the dot product to define precisely the true transit time. The logic employing the 150 and 15 second ranges was developed to give accurate iteration near transit time yet minimize the number of time consuming iteration between transits.

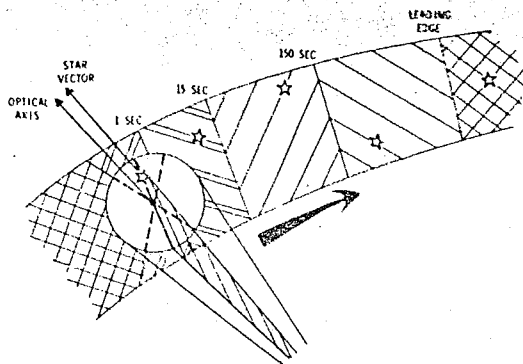


Fig. 6. 3 DOF Simulation Star Field Geometry

The above calculations are done for each star within transit range for each slit. At time of transit, the slit identification is tagged for use in algorithm calculations, and the star identification is tagged for informational print out only.

Whenever the rates change due to limit cycle control, the predictions are no longer accurate and the entire table of transit times are re-predicted. Note that the above logic applies only to the truth model; the SPARS algorithms do not predict transits before they occur, but respond only after a transit signal is received from one of the star sensors.

Attitude and Limit Cycle Solution

The truth model implements a highly accurate attitude solution by using a fourth order Runge Kutta integration of true rate. This true

attitude is used for star transit generation, attitude error calculation, and true rate generation. A modified vehicle limit cycle model changes rate as though a reaction control jet fired whenever an attitude deadband limit is exceeded. Unlike a true vehicle attitude controller, the simulated jet firings continue until the limit cycle rate magnitude exceeds some minimum. Thus, a worst case vehicle rate is simulated.

Sensor Error Models

The star sensor error model consists of fixed errors in the knowledge of star sensor geometry and detector slit orientations, simulating calibration uncertainties, and random errors to simulate variations in threshold transit time detection, non-planar slits, and noise in the star sensor processing electronics. This additive random noise has a normal distribution with a variance equal to that expected of the star sensors.

The gyro drift model simulates three components. They are: Constant bias drift, sinusoidal drift and random drift.

In order to define an appropriate model, these components were measured using available computer sampling and data reduction schemes on test gyros. Less emphasis was placed on the first two components since SPARS corrects for the bias as part of the algorithm, and sinusoidal drifts typically occur only during gyro warmup or temperature transients. The latter are small in SPARS due to the active gyro temperature control. Considerable emphasis was given to the modeling of gyro random drift, however, because of its importance in performance evaluation. It is shown in Ref. 4 that the random drift of the SPARS gyros can very closely be represented by white noise over the frequency spectrum of interest. Thus, a model for white noise gyro drift was developed. The following are considerations of this development.

For times much longer than the random gyro drift correlation time (i. e., longer than the longest gyro drift autocorrelation function time constant, which is usually quite short), it is shown in Ref. 8 that:

$$E[\Delta\theta^2(t)] = 2\pi G_{xx}(0) t \quad (35)$$

where $\Delta\theta(t)$ is the attitude error due to gyro drift, $G_{xx}(0)$ denotes power spectral density at zero frequency, t is time and E denotes expectation. This shows that the long period variance of the integral of exponentially correlated gyro drift is proportional to the product of the power spectral density at zero frequency and time. It is not possible to simulate this phenomena directly with white noise on a digital computer, due to the fact that a finite integration step size must be used. The method of introducing random rate error $\Delta\omega_i$ in the SPARS simulation can be represented by the block diagram of Fig. 7.

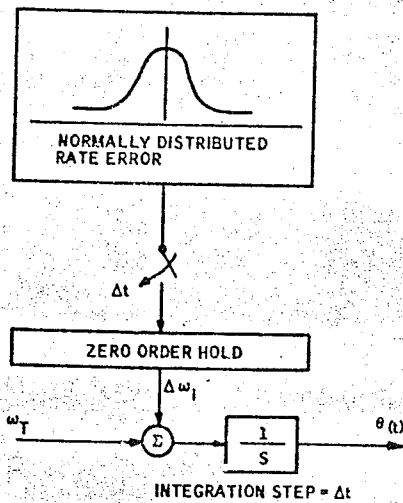


Fig. 7. Random Gyro Drift Simulation

The incremental attitude error incurred during any given period Δt is

$$\Delta \theta_1 = \Delta \omega_1 \Delta t \quad (36)$$

and, since the individual rate error samples are uncorrelated, the Central Limit Theorem can be invoked to give the error after a time $t = n \Delta t$:

$$\begin{aligned} \theta_1(t) &= \sum_{i=1}^n \Delta \theta_1 \\ &= \Delta t \sum_{i=1}^n \Delta \omega_1 \end{aligned} \quad (37)$$

which leads to the variance equation

$$E[\Delta \theta^2(t)] = n \Delta t^2 E(\Delta \omega^2) \quad (38)$$

Equations (35) and (38) lead to the following relation which must be satisfied by the digital simulation

$$[E(\Delta \omega^2)]^{1/2} = \left(\frac{2\pi G_{xx}(0)}{\Delta t} \right)^{1/2} \quad (39)$$

However, a gyro specification is not always written in terms of the zero-frequency power spectral density, but more often in terms of its integral to some frequency, ω_c .

$$\int_{-\omega_c}^{\omega_c} \text{PSD} = \int_{-\omega_c}^{\omega_c} G_{xx}(o) d\omega = 2\omega_c G_{xx}(0) \quad (40)$$

so

$$[E(\Delta \omega^2)]^{1/2} = \left(\frac{\pi \int \text{PSD}}{\Delta t |\omega_c|} \right)^{1/2} \quad (41)$$

or

$$[E(\Delta \omega^2)]^{1/2} = \left(\frac{\int \text{PSD}}{2\Delta t |fc|} \right)^{1/2} \quad (42)$$

where $fc = \omega_c/2\pi$. As an example, consider a one second truth model integration step size and $|fc| = 0.5$ Hz. These values yield the required standard deviation for the rate power spectral density:

$$[E(\Delta \omega^2)]^{1/2} = (\int \text{PSD})^{1/2} \quad (43)$$

Notice that if the integration step size were changed to 0.1 second, the rate power spectral density would have to be changed to

$$[E(\Delta \omega^2)]^{1/2} = \sqrt{10} (\int \text{PSD})^{1/2} \quad (44)$$

to yield the same simulation results. Equation (42) defines the required standard deviation input scaling of the gaussian random number generator used in the SPARS simulation for modeling gyro drift.

The simulated gyro drift is added to true rate to g , measured rate. This is then quantized into an integral number of weighted pulses for input to the system and the remainder after quantization is added to measured rate in the next sampling interval.

Error Processing Technique

Attitude error is computed during the simulation run and stored on magnetic tape with many other system variables for display and input to the many analysis routines available. A running RMS of the attitude errors is also generated in the simulation to indicate one sigma (over time) performance.

This simulation was programmed using the Honeywell-developed COMRADE (COMputer-Aided-DEsign) system which operates on a hybrid computer. This is an extensive on-line executive system that provides the user with a man-machine communication link, enabling the engineer to control the computer through a repertoire of simple commands. These commands permit the user to control all of the input-output devices, run programs, adjust input data, and graph data on a display scope. Emphasis is placed on man-in-the-loop decision making at a modest sacrifice in computer utilization efficiency. The SPARS simulation has been incorporated within the framework of the COMRADE system to allow simple and rapid changes to system parameters, immediate display of results, and evaluation of results using them as inputs to many other statistical and spectral analysis programs. A list of input

parameters that can be varied in the simulation to investigate system performance is given in Table 1.

More than 45 standard analysis routines are available in the COMRADE program library. Several of these which have been particularly useful to the analysis of SPARS system errors and gyro drift data are described in Table 2.

Table 1. List of Simulation Input Parameters

| |
|---|
| Initial attitude error |
| Initial rate error |
| Limit cycle rate (three axes) |
| Limit cycle excursion angles (three axes) |
| Attitude jet thrust time and time constant |
| Star sensor random error |
| Gyro pulse weight |
| Gyro precounter sampling frequency |
| Fixed point attitude solution word length |
| Detectable star magnitude |
| Gyro fixed bias |
| Recursive filtering parameters |
| False star transits and star catalog errors |
| Gyro random drift |
| Star sensor and detector geometry |
| Tolerance multiplication factor |

Table 2. Useful COMRADE Library Programs

| Name | Description |
|----------|---|
| AUTOCOR | Computes mean, variance, intensity, linear trend, autocorrelation function, spectral density estimates, and spectral density estimates convolved with the Hamming spectral window on a set of data samples. |
| FOURIER | Computes the Fourier line spectrum on a set of data samples using the Cooley and Tukey Fast Fourier Tran. form. |
| LPRINT | Prints a rapid, low resolution graphical copy of any x-y pair. |
| PROBDENS | Computes mean, intensity, variance probability density function (PDF) and the PDF integral on a set of data samples. |
| SAMPLE | Generates a set of data samples by periodically sampling from one to five analog signals at a specified rate. |

ANALYSIS AND SIMULATION RESULTS

During the past two and a half years on the SPARS program, a large amount of analytical and computer simulation results have been compiled, in addition to the actual component and system testing efforts. This section will describe a few of the more interesting and unique analysis and simulation results.

Single-axis Analytical Results

A single-axis analytical approach has been used on SPARS to gain initial insight into the

general error propagation characteristics of the strapdown mechanization, and to evaluate the effects of gross system parameter changes prior to detailed computer simulation. In essence, the steady state or quasi-steady state Riccati equation and related steady state stochastic equations can be manipulated to yield RMS dynamic attitude error values for updated attitude reference systems. These equations can also be manipulated to yield the required values of star sensor accuracy or star transit interval for a given level of system accuracy. This analysis is performed on a single-axis basis. Certain plausible multipliers can be introduced to obtain three-axis performance estimates.

The steady-state performance of a system with gyros can be bounded quite easily from above and below. The lower bound is obtained by assuming constant star transit intervals and an optimal linear filtering mechanization. The upper bound is obtained with a realistic star transit frequency distribution (zero-order Poisson) and a particular nonoptimal filtering solution; namely, an attitude gain of one. Let P be the attitude error variance. Then between star transits, the equation describing the buildup of the variance is

$$P_{n-} = P_{n-1+} + Q\Delta t_{AV} \quad (45)$$

where Q is the zero-frequency power spectral density of the gyro drift and Δt_{AV} is the time between transits. At a transit, the optimal attitude gain is

$$K_n = P_{n-} H^T [H P_{n-} H^T + R]^{-1} = \frac{P_{n-}}{P_{n-} + R} \quad (46)$$

where $H=1$ for this single-axis system and R is the star sensor error variance. The attitude variance update is then described by

$$\begin{aligned} P_{n+} &= (1 - K_n H) P_{n-} \\ &= \left[1 - \frac{P_{n-}}{P_{n-} + R} \right] P_{n-} \\ &= \frac{P_{n-} R}{P_{n-} + R} \end{aligned} \quad (47)$$

Now, the crucial step is in recognizing that for steady-state operation and constant star transit intervals,

$$P_{n-1+} = P_{n+} \quad (48)$$

Thus, substituting Eq. (47) into Eq. (45) using (48),

$$P_{n-} = \frac{P_{n-} R}{P_{n-} + R} + Q\Delta t_{AV} \quad (49)$$

where the N have been dropped because they are now redundant. Eq. (49) is a quadratic equation in P- :

$$P_-^2 - P_- Q \Delta t_{AV} - R Q \Delta t_{AV} = 0 \quad (50)$$

Eq. (50) clearly has only one positive solution. The attitude error variance picture shown in Fig. 8 can now be drawn.

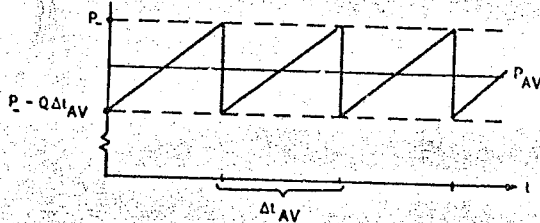


Fig. 8. Attitude Error Variance Behavior (Lower Bound)

The mean-square single-axis attitude error P_{AV} is given by

$$P_{AV} = P_- - \frac{Q \Delta t_{AV}}{2} \quad (51)$$

$$= \left(\frac{Q^2 \Delta t_{AV}^2}{4} + R Q \Delta t_{AV} \right)^{1/2}$$

This is the single-axis attitude error lower bound. It is optimistic because of the equal star transit interval assumption.

The upper bound is obtained by a quite different approach; by using the attitude gain = one mechanization, and assuming that the star transit interval spacing is Poisson distributed. (This is a pretty good assumption. Also note that the star transit interval correlation plays no role in this discussion). In this case, the attitude variance propagates after a transit like

$$P = R + Qt \quad (52)$$

Since the star transit intervals are zero-order Poisson distributed, the star transit interval probability density function is

$$P(\Delta t) = \frac{1}{\Delta t_{AV}} e^{-\frac{\Delta t}{\Delta t_{AV}}} \quad (53)$$

where Δt_{AV} is the same number as in the constant transit interval discussion. Now, the probability density function for being in the transit interval whose length is between t and t+ Δt at any particular time is then given by the first-order Poisson distribution

$$P(\Delta t) = \frac{\Delta t}{(\Delta t_{AV})^2} e^{-\frac{\Delta t}{\Delta t_{AV}}} \quad (54)$$

During any particular transit interval, the average attitude variance is

$$P_{AV, INT.} = R + \frac{Q t}{2} \quad (55)$$

Therefore, integrating over all possible interval lengths

$$P_{AV} = \int_0^{\infty} \left(R + \frac{Q t}{2} \right) \frac{1}{(\Delta t_{AV})^2} e^{-\frac{t}{\Delta t_{AV}}} dt \quad (56)$$

$$= \frac{R}{(\Delta t_{AV})^2} \int_0^{\infty} t e^{-t/\Delta t_{AV}} dt + \frac{Q}{2(\Delta t_{AV})^2} \int_0^{\infty} t^2 e^{-t/\Delta t_{AV}} dt$$

$$= R + Q \Delta t_{AV}$$

(Notice that if the transit interval spacing was uniform instead of Poisson, the average attitude variance would be $R + Q \Delta t_{AV}/2$. This is an important point, as it shows the effect of interval distribution.) This is the single-axis attitude error upper bound. It is a conservative estimate because of the nonoptimal filtering assumption. Therefore:

$$\left(\frac{Q^2 \Delta t_{AV}^2}{4} + R Q \Delta t_{AV} \right)^{1/4} \leq (P_{AV})_{TRUE}^{1/2} \leq (R + Q \Delta t_{AV})^{1/2} \quad (57)$$

Equations (51) and (56) are the equations of interest, as parametric curves can now be drawn for such things as star transit interval. One word of caution. For wide fields of view, more slits will tend to smooth out the interval irregularities and the attitude accuracy will approach the lower bound. However for small fields of view, this will not be true, since the interval distribution will remain Poisson no matter how many slits are added. (Of course, Δt_{AV} will go down though).

The above approach to parametric analysis is valid only for a single-axis system. However, to get a good idea of three axis performance, multiply the answers by 3, i. e., $\sqrt{3} \times \sqrt{3}$. One of the $\sqrt{3}$ factors comes from the fact that each of the single-axis errors will be about the same order of magnitude. Thus the vector sum would be $\sqrt{3}$ times any single component. The other factor of $\sqrt{3}$ comes from the fact that the average sensitivity (H) of attitude error in one axis to a given transit is not one, but a number like $1/\sqrt{3}$.

This approach to determining attitude reference performance and the parametric impact of transit interval and star sensor accuracy, yields a rapid inexpensive "ball-park" estimate which defines the limits of system performance. In problems where it is required to define a level of performance in a short time, such as in proposal exercises, it allows the investigator to remain in close contact with the essence of the problem, rather than becoming embroiled in completely unrelated problems involved with getting

a complex simulation modified and operational in a short time, and minimizes the possibility of error, since the answers are easily checked.

The method provided a guide in SPARS for selection of input parameters for the simulation which was more complex and expensive to run.

Star-Transit Interval Study

A comprehensive computer study of the star-transit interval characteristics of candidate SPARS strapdown star sensors has been conducted to identify parametric relationships and the extreme frequency variations possible. To establish limits on potential system errors between star sightings in the SPARS, which utilizes body-fixed star sensors on a rotating vehicle with (drifting) gyros for interpolation between sightings, it is important to know how the interval between star sightings may vary. To optimize sensor and system design, interval variation as a function of star magnitude, sensor FOV, sensor orientation, and orbit orientations must be known. A computer analysis on transit intervals was therefore conducted early in the Phase 0 study (Ref. 3).

The analysis was made for a satellite in a near-polar orbit, with a pitch motion of 240 deg/hr. Star data were obtained from the Smithsonian star catalog (Ref. 9). To gain insight into the effect of orbit orientation, six equally spaced line-of-node arguments were used. For each of these, runs were made for four limiting star magnitudes. Since the initial objective was to bound the problem and determine trends, a typical star sensor configuration was used, namely two sensors with single slits, both pointed 30 degrees off vertical to the same side of the orbit plane and at an angle of 60 degrees to each other in that plane. Runs (swaths) were made with the sensors pointing in turn to both sides of the orbit plane. Sensor FOV was varied from 2 to 10 degrees.

The analysis consisted of averaging the time interval between star-slit transits over one orbit for one set of parameters. The summary results of this analysis are given in Fig. 9. In Fig. 9 the lower and upper bounding lines represent the best and worst star swaths found, respectively. (The worst swath is not necessarily the same one for different FOV's or limiting magnitudes). The line in the center of each spread represents the mean time between transits for all swaths at that magnitude. The spread indicates the range of values resulting from the six different line-of-node orientations. If a larger number of swaths had been used, the mean points would fall more exactly on a straight, 45-deg line for small FOV's. That is, for a sufficiently large statistical sample, as the FOV is doubled, the average time between star transits is halved. These results show that for the baseline optical system the average time between star transits for all orbits is 210 sec. For the extreme orbits, this varies between 160 and 340 seconds.

Dynamic Attitude Error Results

The SPARS simulations have identified that the SPARS dynamic error requirement is easily satisfied with the proven performance of GG334A gyros and state-of-the-art star sensors. Single-degree-of-freedom simulation results and the more comprehensive three-degree-of-freedom simulation have shown that there are two primary contributors to the dynamic SPARS attitude error; gyro random drift variance, and star sensor error variance. It is possible - with modest system complexity - to minimize the effect of all other dynamic error sources, such as star transit interval (as shown in Fig. 11), computational roundoff and integration algorithm truncation, gyro pulse weight, fixed drift, and gyro misalignment. Static errors caused by such things as optical misalignments, shifts, and imperfect calibration were analyzed separately.

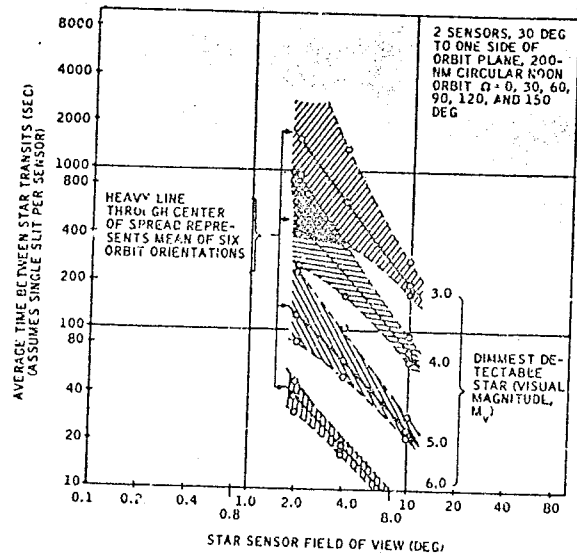


Fig. 9. Star Transit Intervals versus FOV

The effects of the two primary error sources on system performance are shown in Figs. 10 through 12. The normalized three-axis, 1σ attitude reference system dynamic error is shown as a function of the empirical noise parameter U , which is discussed in the SPARS data processing section of this document. U is related to the forward loop gain of the recursive filtering calculations during steady-state operation. The figures show that the optimum system accuracy is a very shallow function of U until a relatively large value is reached. This is in contrast to the results that were obtained early in the study when a random-walk gyro drift model was used. In that case, optimal system performance was quite sensitive to U . However, the

extensive gyro testing (Ref. 4) has shown conclusively that the random-process gyro model being used presently is the correct representation in the frequency range of interest.

The simulation results summarized in Figs. 10 to 12 were used to create design curves for the Phase O star sensor specifications.

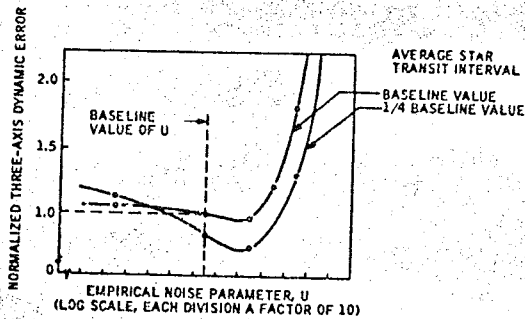


Fig. 10. Effect of Star Transit Interval

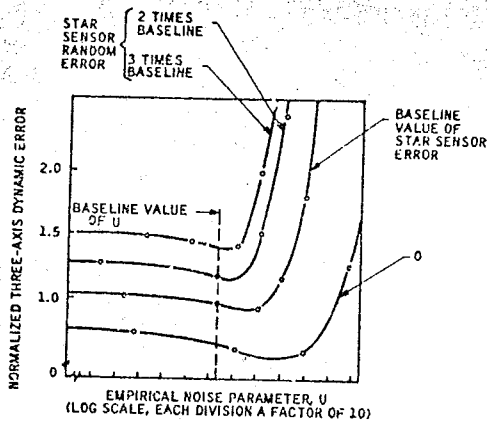


Fig. 11. Effect of Star Sensor Error

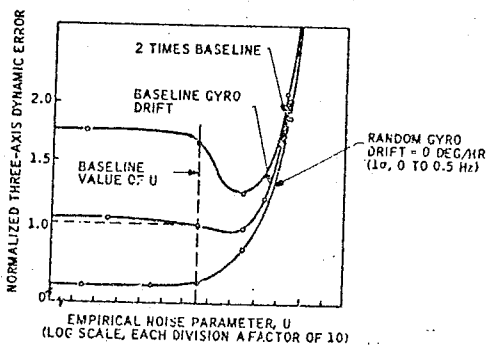


Fig. 11. Effect of Gyro Drift

The baseline system specified in Phase O had an ample margin of meeting the required one sigma accuracy. There were three main reasons for having this margin.

- (1) The 1σ errors shown were computed over many orbits to be truly representative. The system performance statistics are somewhat variable from orbit to orbit due to fluctuations in the filtering equations and variations in the number of stars seen; the baseline mechanization provides sufficient margin to comply with the specified accuracy even for the "worst orbit" condition.
- (2) The primary intent of the 1σ SPARS accuracy requirement is that the system error never exceed three times this value. This is true regardless of attitude error statistical distribution. In the case of SPARS, the attitude error statistics are "steeper" than Gaussian, and sufficient margin is provided to guarantee 3σ performance.
- (3) Sufficient margin was also allowed for static errors, shifts, etc., which were specified as design-to parameters.

The following significant conclusions have been reached:

- (1) The system performance is not sensitive to any nonuniform distribution of stars.
- (2) The GG334 gyro proven performance is more than adequate for SPARS.
- (3) The risk involved, if any, due to the development status of the star sensor is minimized, because the star sensor error is attenuated in its effect on system error.

Star Sensor Geometry Results

The SPARS three-degree-of-freedom simulation results have shown that the attitude reference system error time history is relatively insensitive to the star sensor angular orientations and detector geometries over a broad range of values. Probably the most useful function of the SPARS three degree-of-freedom (3 DOF) simulation at Honeywell has been the determination of the effect of various changes in star sensor geometry and slit configuration. It would be extremely difficult to obtain reasonable estimates of these sensitivities analytically, since the parametric relationships involved are highly nonlinear and often not too intuitive. However, operating in an on-line mode with the SPARS 3 DOF simulation, observing the performance characteristics for various parametric combinations, and making corresponding changes resulted in a rapid determination of the effects of sensor geometry on

system performance. The significant conclusion of this study has been that star sensor geometry, other than the FOV, does not have a strong effect on system performance.

Telescope look-angle studies indicate that there is no apparent performance advantage to having the individual star telescopes cut different star swaths in the celestial sphere. With this being the case, having the telescopes oriented one behind the other eliminated 10 star simulators in the lab test and minimized the star catalog size. The studies further indicated that the out-of-orbit star swath angle and the angle between star telescopes have little effect on performance for a wide range of angles.

Because performance is not a constraint and because there is a severe sun shield penalty for look angles closer than 30 deg to the sun, the telescopes are oriented 60 deg apart. This separation ensures that at least one of the two sensors can see stars at all times without the telescopes having to be oriented closer than 60 deg to the horizon.

The salient results (normalized) of the star sensor slit studies are shown on Fig. 13 for the star sensor geometrical combinations considered. Both one and two sensor configurations were studied. The first two-sensor configuration shown has a single slit in each sensor. The slits are canted at 45 deg to the direction of motion in an attempt to gain attitude information about both axes parallel to the focal plane. The resulting error is seen to be relatively large. The addition of a second slit more than doubles the number of star transits and yields increased pitch axis sensitivity, cutting the attitude error in half. Also shown are the performance results of a number of two-sensor configurations with three slits per sensor. For the first one shown, it is seen that the slit angle has little effect on system performance. The reason for this is that increasing the angle increases the sensitivity to attitude errors about an axis parallel to the direction of motion, but counteracting this is the fact that fewer stars are seen by the canted slits. Several asymmetrical three-slit arrangements were also investigated, and very little change in system performance was observed.

One additional significant result of this study is that configurations with just one star sensor did not perform as badly as might be expected. This result has strong implications on system reliability considerations, since the failure of one of two star sensors would not be catastrophic and a modest performance degradation would be experienced. The reason one might expect a big error when using only one sensor is that the sensitivity of one sensor to attitude errors about its optical axis is quite low. Fortunately, this is compensated for by the fact that this axis keeps changing continually with respect to inertial space, so that three-axis inertial information is ultimately obtained.

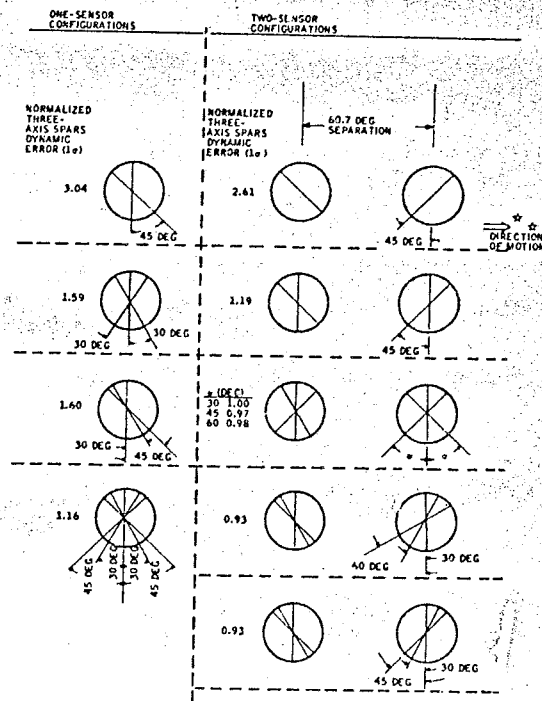


Fig. 13. Effect of Star Sensor Detector Geometry

Computational Error Study

Results obtained with the SPARS three-degree-of-freedom (3 DOF) simulation have demonstrated that the computational errors in attitude calculation are small with respect to other system error contributors when the 1824 computer is used, and that the design value of gyro pulse weight is an optimum value. There are three primary computational contributors to the SPARS attitude error: integration algorithm truncation, roundoff of the numerical values of critical parameters due to finite register length, and the quantization of attitude changes due to the digital rebalance electronics of the gyros. There is a tradeoff between roundoff errors and truncation errors for a given word length and integration algorithm. Longer integration step sizes result in a poorer approximation of the algorithm to the kinematics of the attitude relationships, whereas shorter step sizes result in more computer adds and multiplies per unit time, resulting in more rapid loss of accuracy in the least significant bits of the attitude variables.

The SPARS 3 DOF simulation was used to evaluate integration algorithms and computation step sizes. The first method investigated was a first-order (rectangular) method with a step size of 2.0 sec. The resulting computational drift rate was approximately 0.1 deg/hr. In an effort to reduce this drift to an acceptable value, a second-order Runge-Kutta/improved Euler algorithm was added, resulting in a reduction of the computational drift rate by three orders of magnitude. Operating within the framework of a typical system mechanization, it is important to know what effect this has on the attitude error statistics. Fig. 14a shows the effect of second-order integration step size on SPARS performance. The best performance occurs in the 1-sec range, with the error increasing somewhat sporadically for longer time, and also increasing in the 0.1-sec region as roundoff error starts to come into play. However, this study was done at 39-bit accuracy, and the optimum point will shift to the left for the baseline 48-bit integration in the UNIVAC 1824.

The effect of gyro pulse weight is shown in Fig. 14c. The dotted line is the result that is obtained when the standard deviation of the quantization uncertainty for each gyro ($1/\sqrt{3}$ times the pulse weight) is root-sum-squared with the attitude error at a pulse weight of zero. The actual data are seen to roughly follow this expected trend, with some superimposed "beat frequency" effects resulting from the interplay between pulse weight size and forced limit cycle amplitudes that were used in the simulation to maintain worst-case rates and maximum jet firings. The baseline choice of pulse weight is substantiated by the data.

ACQUISITION STUDIES

Prior to steady-state operation, an acquisition phase is necessary to remove large attitude uncertainties and residual gyro biases. A crude initial vehicle attitude relative to inertial space may be obtained from the orbital ephemeris data and assumed vehicle earth-oriented control. The uncertainties in this computation are directly proportional to the vehicle control system limit cycle amplitude. These could be reduced if the error signals from the separate vehicle control system were used in the initial calculation. Although not necessary, this would reduce acquisition time.

The body attitude solution begins from the initial condition using gyro data and preflight drift compensation coefficients. Initial residual gyro drift uncertainty may be a relatively large constant bias. This is gradually reduced to the level of the random drift by the rate portion of the state corrections as they are made at accepted star transits.

Due to the large initial attitude uncertainty, special logic is required during acquisition. At a star transit, there may be more than one cataloged star within the attitude uncertainty of any given detector slit and more than one slit within the attitude uncertainty of the transiting star. It

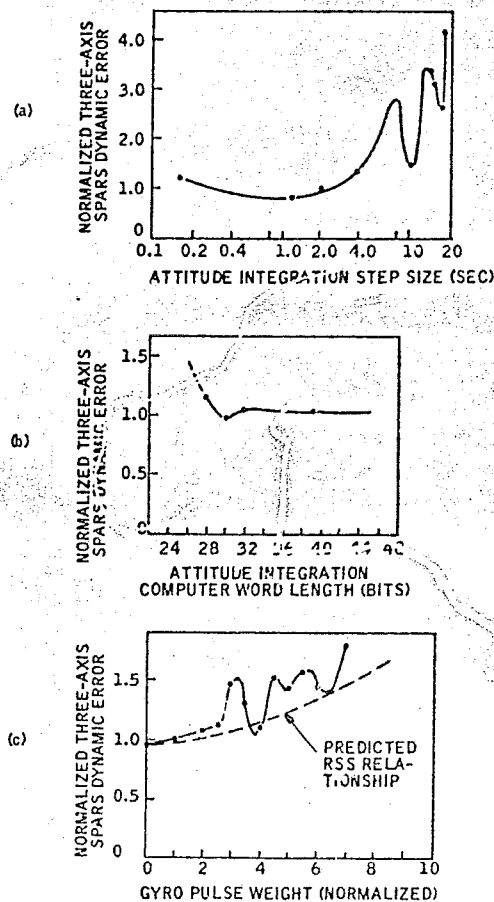


Fig. 14. Computational Effects

is clear from Fig. 15 that if only a single detectable star were within the field of view, there would still be an ambiguity as to which detector was involved in a transit. Thus, acquisition requires a scheme to identify both star and detector at each transit before a state correction can be computed. This is not necessary in steady-state since the attitude uncertainties are extremely small and a small measurement tolerance will sort out the proper slit as well as star. Thus, it is from acquisition that the requirement for a slit identification signal sent from the star sensors to the computer originates.

As mentioned above, there may be several stars at a transit time that are within the attitude uncertainty of the identified detector plane. The catalogued star which gives the smallest dot product (DOT from Eq. 18) is not necessarily the star causing the transit. Applying a state correction from a false star can cause rapid divergence of the attitude error, since this constitutes a

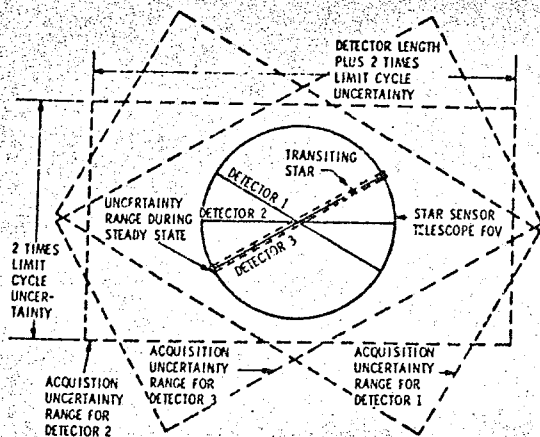


Fig. 15. Acquisition Uncertainty - Detector Not Known

non-linearity in violation of the basic algorithm assumptions. To avoid this, the values of DOT for all candidate stars are tested against a tolerance which represents the maximum expected value of DOT. If more than one star gives a magnitude of DOT within the tolerance, it can be inferred that the stars are spaced too closely for identification and the transit must be neglected. Similarly, if none of the DOT magnitudes are within the tolerance, the transit must be disregarded. The latter case may be due to transiting an uncatalogued star, an illuminated dust or propellant particle, or noise in the detector electronics; in all of these situations no state correction should be made.

The tolerance used in the candidate selection needs to be large at the start of acquisition because of the large attitude uncertainty. As the uncertainty is reduced, the tolerance should also be reduced to minimize the number of rejected transits due to ambiguities, thus increasing the percentage of accepted transits.

The most appropriate time-variant tolerance is

$$T = M \left[\text{HPHT}^T + R \right]^{1/2} \quad (58)$$

where the bracketed quantity is the variance of DOT, and is computed in Eq. 24. The factor, M is a constant multiplier. The quantity HPHT^T is that portion of the variance in DOT due to attitude uncertainties, and R is that portion due to measurement uncertainties within the sensor itself. The multiplier, M, boosts up the tolerance to cover the full range of possible measurement values since $[\text{HPHT}^T + R]^{1/2}$ is a one-sigma uncertainty and thus is often smaller than the actual error.

Initially the values in the P matrix are large to represent initial condition uncertainties. These values diminish at each state correction, consistent with expected system error. When steady-state performance is reached the covariance matrix terms are small and T approaches the level of $R^{1/2}$, resulting in acceptance of nearly every valid transit. T will not tend to zero because of the constant variance R and the plant noise term added to prevent the terms in P from diminishing to zero.

An illustrative example of the dot product and tolerance convergence is shown in Fig. 16. The dot product and tolerance generally decrease at each state correction but the tolerance is always greater than the correct dot product at each valid transit.

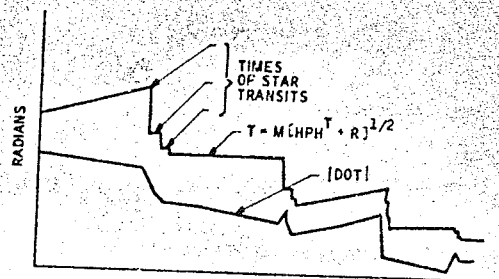


Fig. 16. Example of DOT Product and Tolerance Convergence

Despite the logic to guard against false transits, a small probability still exists that a transit can be incorrectly identified. This results when a transit from an uncatalogued star, dust particle, etc. occurs and a DOT from one and only one catalogued star is less than the tolerance at that time. The result is an incorrect state correction, which usually causes increased system error; yet the covariance matrix and hence the tolerance for accepting future transits decreases as if the correction were made on the correct star. Further transits may be rejected or falsely identified due to the correct star being outside the reduced acceptability tolerance. In most cases this causes the system error to increase rapidly as shown in Fig. 17, due to gyro bias compensation errors. In a few cases the attitude error is excessive but not diverging, and is characterized by continued rejection of future star transits. Fig. 18 is an example of this tolerance/dot product relationship. System error could remain outside the tolerance without diverging if a means were not provided for sensing and correcting the situation.

Two methods are used to test for excessive attitude error. The first is a comparison of system Euler angles to a crude attitude based on orbital ephemeris. If the difference for any one axis is greater than that expected from limit cycle and ephemeris uncertainties, the acquisition process is restarted. Should the attitude error

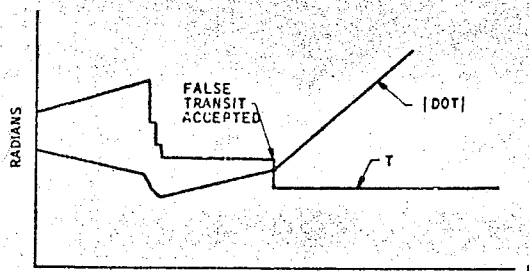


Fig. 17. Example of Attitude Divergence After Acceptance of False Transit

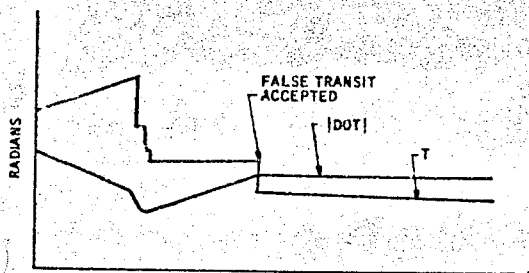


Fig. 18. Example of Excessive Attitude Error After Acceptance of False Transit

become large enough to cause rejection of transits on the basis of tolerance, but not sufficiently large as to cause restart by the above method, a second method is used. It is a test on the number of successive transits for which there are no DOT's from catalogued stars within the tolerances. A few such transits must be permitted to allow for uncatalogued stars and false transit signals. Rejected transits based on more than one DOT within the tolerance should not be included in the count to determine restart, since this often occurs in the early stages of convergence in a fairly dense portion of the sky. However, many zero candidate transits in succession indicate that the error estimates are lower than the actual errors and the acquisition process must be restarted.

The simulation program previously described was used to study convergence time sensitivities to initial conditions and system parameters. A plot of convergence time versus initial condition uncertainties is shown in Fig. 19. In general, the convergence time increases as the initial attitude errors increase. Sensitivity to changes in initial drift compensation errors was small except for the worst case 2-1/4 degree and 0.5 degree/hour error condition. (Convergence time with zero initial errors was not zero because the initially large covariance matrix causes early corrections to be excessive). Convergence times can be further reduced when the initial uncertainties are reduced if a corresponding reduction is made in the initial covariance matrix.

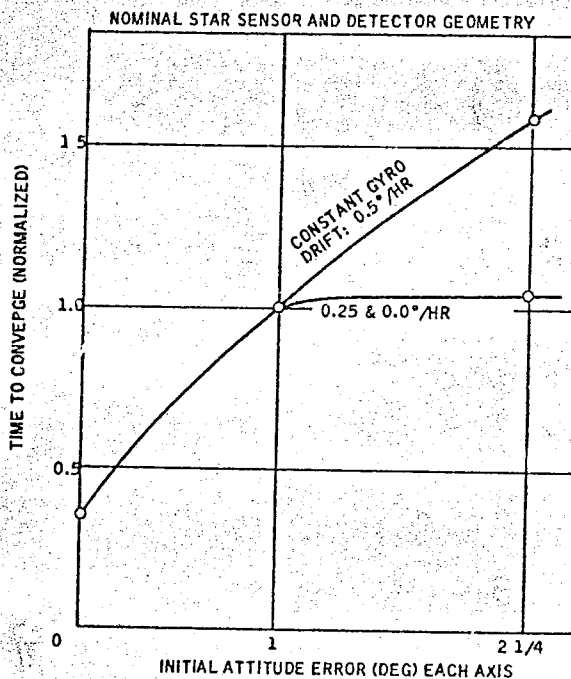


Fig. 19. Convergence versus Initial Condition Uncertainties

Simulation runs were made to investigate two aspects of the effect of star sensor detector sensitivity; 1) the effect of the number of detectable stars as established by detector sensitivity, and 2) the effect of a difference between the number of catalogued stars and the number of detectable stars.

One would expect that as the number of detectable stars increases, convergence time will decrease, simply because attitude measurements become more frequent. However, as the number of detectable stars is further increased, a point will be reached where convergence time begins to increase again due to rejections of multiple transit candidates within the tolerance. Results of simulation runs indicated that this latter effect was not a significant factor over the range of detector sensitivities being considered. In fact, the effect of the number of detectable stars was found to be much less important than the difference between the number of detectable and catalogued stars.

The effect of such a difference is shown in Fig. 20. These data were obtained by varying the number of detectable stars while holding fixed the number of catalogued stars. The results, as expected, indicate that the better the assessment of which stars the detector can "see", the faster the acquisition process.

Simulation data was also obtained to show sensitivity of convergence time to star sensor field of view (FOV). The results, shown in Fig. 21, indicate that a large FOV is desirable from

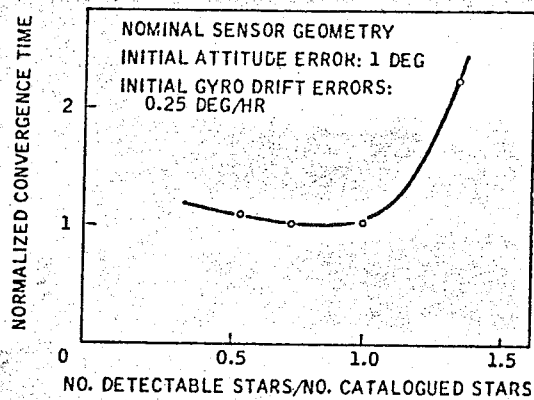


Fig. 20. Convergence Time versus Detector Sensitivity

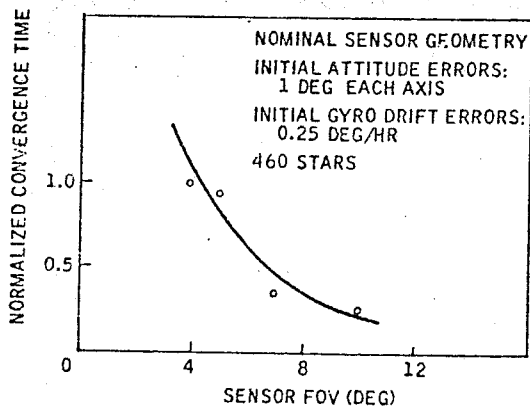


Fig. 21. Convergence Time versus Sensor FOV

an acquisition standpoint. However, this must be traded off against other considerations such as accuracy, the "window required in the spacecraft," and sun baffling, all of which pose problems at large fields of view.

CONCLUSION

The SPARS algorithms described herein have been proven in digital simulation and real time system test. During the tests performed in Phase IA, the algorithms were implemented on an SDS-9300 computer. Most of the algorithms were programmed in Fortran, with the exception of input/output interrupt servicing routines. Considerable knowledge was gained in handling the

problems of interrupts, which is a critical area in SPARS computations. That knowledge is currently being applied in Phase IB to program the SPARS algorithms for the UNIVAC 1324C flight computer. Laboratory tests will begin in early 1970 using the programmed 1824 with a complete SPARS prototype (Ref. 10). The SPARS algorithms are also being programmed for a Honeywell DDP-516 computer for real time solution in parallel with the 1824.

An estimate of the computational requirements for the 1824 computer is given in Table 3. This shows that the SPARS algorithms require less than half of the capacity of this computer from both a storage and speed standpoint. Thus, the SPARS can be implemented in a flight vehicle with a typical aerospace general purpose computer with plenty of space and time remaining for other computational functions (e.g., vehicle control, experiment pointing, etc.).

The simulation program described herein has been a powerful tool in analyzing SPARS performance and delimiting design parameters. The simulation results presented have shown that the SPARS dynamic errors are within the requirements of the SPARS program for state-of-the-art components. Needless to say, the simulation data, as well as test data, have proved the feasibility of the SPARS algorithms.

Table 3. SPARS Computational Requirements

| Task Module | 24 Bit Words | | Request Time/Cycle | Percentage of Computer Time Used |
|-----------------------------|--------------|------|--------------------|----------------------------------|
| | DRM | NDRM | | |
| Executive | 20 | 400 | 0.5 ms/Zms | 14.0 |
| Event Data Processing | 80 | 150 | 15 μ s/100 ms | 5.0 |
| Star Sensor Data Processing | --- | --- | --- | --- |
| Star Catalog | --- | 1000 | --- | 0.4 |
| Sorting | --- | 200 | 10 ms/star transit | 0.6 |
| Recursive Filter | 160 | 1000 | 50 ms/star transit | --- |
| Program Constants | --- | 300 | --- | --- |
| Totals | 200 | 2050 | --- | 30.0 |
| UNIVAC 1824 C | 512 | 8192 | --- | 100.0 |

DRM - destructive readout memory
NDRM - non-destructive readout memory

APPENDIX A

DERIVATION OF GEOMETRY MATRIX

The geometry matrix, H, is defined as the matrix of partial derivatives relating perturbations in state to perturbations in measurement. Thus:

$$\delta(\text{DOT}) = [H] \delta \vec{x} \quad (\text{A1})$$

where

$$H_i = \frac{\partial}{\partial x_i} (\text{DOT}) \quad (i = 1-6) \quad (\text{A2})$$

$$\text{and} \quad \text{DOT} = \vec{1}^B_N \bullet \left\{ [T_{BI}(t)] \vec{S}^I \right\} \quad (\text{A3})$$

which is the dot product of the unit normal vector to the detector slit plane, \bar{i}_N^B , in body coordinates and the unit vector to the star ray, \bar{S}^I , in the inertial coordinate frame transformed to body coordinates thru $[T_{BI}]$. The dot product represents the one dimensional angular error (small angle approximation) in the transformation matrix $[T_{BI}]$ at the measured time of transit.

Evaluating (A2) yields

$$H_i = \frac{\partial}{\partial x_i} \left\{ \bar{i}_N^B \cdot \left[[T_{BI}(t)] \bar{S}^I \right] \right\} \\ = \bar{i}_N^B \cdot \left\{ \frac{\partial}{\partial x_i} [T_{BI}(t)] \bar{S}^I \right\} \quad (A4)$$

(i = 1-6)

Operation on text Eq. (21) yields the partial derivatives:

$$\frac{\partial}{\partial \phi} [T_{BI}] = [G_\phi] [T_{OI}] \quad (A5)$$

$$= \begin{bmatrix} v_1 \sin \psi & v_2 \sin \psi & v_3 \sin \psi \\ \mu_2 \sin \theta & v_2 \cos \psi & \mu_2 \cos \theta \\ v_2 \sin \theta & -\cos \phi & v_2 \cos \theta \end{bmatrix} [T_{OI}]$$

$$\frac{\partial}{\partial \theta} [T_{BI}] = [G_\theta] [T_{OI}] \quad (A6)$$

$$= \begin{bmatrix} \lambda_3 & 0 & -\lambda_1 \\ \mu_3 & 0 & -\mu_1 \\ v_3 & 0 & -v_1 \end{bmatrix} [T_{OI}]$$

$$\frac{\partial}{\partial \psi} [T_{BI}] = [G_\psi] [T_{OI}] \quad (A7)$$

$$= \begin{bmatrix} \mu_1 & \mu_2 & \mu_3 \\ -\lambda_1 & -\lambda_2 & -\lambda_3 \\ 0 & 0 & 0 \end{bmatrix} [T_{OI}]$$

$$\frac{\partial}{\partial B_x} [T_{BI}] = \frac{\partial}{\partial B_y} [T_{BI}] \\ = \frac{\partial}{\partial B_z} [T_{BI}] = 0 \quad (A8)$$

where λ_i , μ_i , and v_i are direction cosines between the body x, y, and z axes, respectively, and the i^{th} axis of the orbit oriented inertial coordinate frame (i = 1, 2, 3), and ϕ , θ , and ψ are the inertial Euler angles roll, pitch, and yaw, respectively.

The geometry matrix then becomes

$$H_i = \bar{i}_N^B \cdot \left\{ [G_i] [T_{OI}] \bar{S}^I \right\}, \quad i = \phi, \theta, \psi \quad (A9)$$

$$[H] = [H_\phi \ H_\theta \ H_\psi \ 0 \ 0 \ 0]$$

APPENDIX B

DERIVATION OF TRANSITION MATRIX

The linearized state vector elements have been defined as perturbations from the non linear solution values of three Euler angles and three body rates

$$\bar{x} = \delta \begin{bmatrix} \phi \\ \theta \\ \psi \\ p \\ q \\ r \end{bmatrix} \quad (B1)$$

It is desired to define the fundamental matrix, $[F]$, in the solution of the linearized state propagation equation

$$\frac{d}{dt} \bar{x} = [F] \bar{x} \quad (B2)$$

since that matrix is required for determination of the transition matrix, Φ .

The Euler angles ϕ , θ , ψ relate the angular position of the body relative to an orbit oriented reference frame. Since the body rotates thru 2 radians in pitch and only very small angles in the other two axes, a pitch-roll-yaw sequence was chosen to avoid singularities.

To obtain the relation between Euler rates and body rates, consider the infinitesimal rotation $\delta \bar{n}$ about some axis. This can be represented with components:

$$\delta \bar{n} = \delta \theta \bar{J} + \delta \phi \bar{I}' + \delta \psi \bar{K}'' \quad (B3)$$

where \bar{I} , \bar{J} , and \bar{K} are an orthogonal right hand triad fixed in the orbital reference frame,

\bar{i} , \bar{j} , and \bar{k} are a similar triad fixed in the body and the primes indicate convenient intermediate frames. The vectors \bar{J} , \bar{I}' , and \bar{K}'' can be represented in terms of \bar{i} , \bar{j} , and \bar{k} as follows:

$$\bar{J} = \bar{J}' \cos \phi - \bar{k} \sin \phi \\ \bar{I}' = \bar{i} \cos \psi - \bar{j} \sin \psi \quad (B4) \\ \bar{K}'' = \bar{k} \\ \bar{J}' = \bar{j} \cos \psi + \bar{i} \sin \psi$$

Substituting these into Eq. (B3) gives

$$\begin{aligned} \delta \bar{n} &= \delta \theta (\bar{j} \cos \psi \cos \phi + \bar{i} \sin \psi \cos \phi \\ &\quad - \bar{k} \sin \phi) \\ &\quad + \delta \phi (\bar{i} \cos \psi - \bar{j} \sin \psi) + \delta \psi \bar{k} \\ &= (\delta \theta \sin \psi \cos \phi + \delta \phi \cos \psi) \bar{i} \\ &\quad + (\delta \theta \cos \psi \cos \phi - \delta \phi \sin \psi) \bar{j} \\ &\quad + (-\delta \theta \sin \phi + \delta \psi) \bar{k} \end{aligned} \quad (B5)$$

Dividing both sides of Eq. (B5) by δt and taking the limit as δt goes to zero

$$\begin{aligned} \frac{d\bar{n}}{dt} &= (\dot{\theta} \sin \psi \cos \phi + \dot{\phi} \cos \psi) \bar{i} \\ &\quad + (\dot{\theta} \cos \psi \cos \phi - \dot{\phi} \sin \psi) \bar{j} \\ &\quad + (-\dot{\theta} \sin \phi + \dot{\psi}) \bar{k} \end{aligned} \quad (B6)$$

But the \bar{i} , \bar{j} , \bar{k} components of $\frac{d\bar{n}}{dt}$ are just the body rates p , q , and r respectively:

$$\begin{aligned} p &= \dot{\theta} \sin \psi \cos \phi + \dot{\phi} \cos \psi \\ q &= \dot{\theta} \cos \psi \cos \phi - \dot{\phi} \sin \psi \\ r &= -\dot{\theta} \sin \phi + \dot{\psi} \end{aligned} \quad (B7)$$

Finally solving Eq. (B7) the Euler rates are

$$\begin{aligned} \dot{\phi} &= p \cos \psi - q \sin \psi \\ \dot{\theta} &= (p \sin \psi + q \cos \psi) \frac{1}{\cos \psi} \\ \dot{\psi} &= r + \tan \phi (q \cos \psi + p \sin \psi) \end{aligned} \quad (B8)$$

Let

$$\begin{aligned} p &= p_m + B_x \\ q &= q_m + B_y \\ r &= r_m + B_z \end{aligned} \quad (B9)$$

where p_m , q_m , and r_m are the measured rates and B_x , B_y , and B_z are the compensation terms for constant gyro bias, which are determined initially in calibration but which are desired to be updated as part of the state vector.

Then upon linearization

$$\begin{aligned} \Delta p &= \Delta B_x \\ \Delta q &= \Delta B_y \\ \Delta r &= \Delta B_z \end{aligned} \quad (B10)$$

Expanding Eq. (B6) in a Taylor series evaluated at a reference which includes limit cycling and taking only first order terms

$$\begin{aligned} \Delta \dot{\phi} &= \frac{d}{dt} \Delta \phi = -p \sin \psi \Delta \psi - q \cos \psi \Delta \psi + \cos \psi \Delta p - \sin \psi \Delta q \\ \Delta \dot{\theta} &= \frac{d}{dt} \Delta \theta = (p \sin \psi + q \cos \psi) \frac{\sin \phi}{\cos^2 \phi} \Delta \phi \\ &\quad + \frac{1}{\cos \phi} (p \cos \psi \Delta \psi - q \sin \psi \Delta \psi + \sin \psi \Delta p + \cos \psi \Delta q) \\ \Delta \dot{\psi} &= \frac{d}{dt} \Delta \psi = \sec^2 \phi (q \cos \psi + p \sin \psi) \Delta \phi \\ &\quad + \tan \phi (-q \sin \psi \Delta \psi + p \cos \psi \Delta \psi + \sin \psi \Delta p \\ &\quad + \cos \psi \Delta q) + \Delta r \end{aligned} \quad (B11)$$

The linearized state equation $\dot{\bar{X}} = [F] \bar{X}$ in matrix form is then

$$\frac{d}{dt} \begin{bmatrix} \Delta \phi \\ \Delta \theta \\ \Delta \psi \\ \Delta B_x \\ \Delta B_y \\ \Delta B_z \end{bmatrix} = \begin{bmatrix} 0 & 0 & 0 & 0 & 0 & 0 \\ p \sin \psi + q \cos \psi \frac{\sin \phi}{\cos^2 \phi} & \frac{1}{\cos \phi} (p \cos \psi - q \sin \psi) & \cos \psi & -\sin \psi & 0 & 0 \\ (q \cos \psi + p \sin \psi) \sec^2 \phi & \tan \phi (-q \sin \psi + p \cos \psi) & \sin \psi & \cos \psi & 0 & 0 \\ 0 & 0 & 0 & 0 & 0 & 1 \\ 0 & 0 & 0 & 0 & 0 & 0 \\ 0 & 0 & 0 & 0 & 0 & 0 \end{bmatrix} \begin{bmatrix} \Delta \phi \\ \Delta \theta \\ \Delta \psi \\ \Delta B_x \\ \Delta B_y \\ \Delta B_z \end{bmatrix} \quad (B12)$$

The solution of the transition matrix, $[\Phi(t; t_0)]$, makes use of this same matrix, $[F]$, and is well known to be

$$\frac{d}{dt} [\Phi(t; t_0)] = [F] [\Phi(t; t_0)] \quad (B13)$$

where $[\Phi(t_0; t_0)] = I$, the identity matrix, which is initialized at every star transit. By taking advantage of the many zero elements of $[F]$ Eq. (B13) can be written

$$\begin{aligned} \dot{\Phi}_{1,j} &= F_{1,3} \Phi_{3,j} + F_{1,4} \Phi_{4,j} + F_{1,5} \Phi_{5,j} \\ \dot{\Phi}_{2,j} &= F_{2,1} \Phi_{1,j} + F_{2,3} \Phi_{3,j} + F_{2,4} \Phi_{4,j} \\ &\quad + F_{2,5} \Phi_{5,j} \\ \dot{\Phi}_{3,j} &= F_{3,1} \Phi_{1,j} + F_{3,3} \Phi_{3,j} + F_{3,4} \Phi_{4,j} \\ &\quad + F_{3,5} \Phi_{5,j} + \Phi_{6,j} \\ \dot{\Phi}_{4,j} &= \dot{\Phi}_{5,j} = \dot{\Phi}_{6,j} = 0 \end{aligned} \quad (B14)$$

$j = 1, 2, \dots, 6$

APPENDIX C

DERIVATION OF THE "NOISE MATRIX," $U(t)$

The propagation of white plant noise in the discrete case of linear recursive filtering can be expressed in the following form

$$U(t) = \int_{t_k}^t \Phi(t, \tau) Q(\tau) \Phi^T(t, \tau) d\tau \quad (C1)$$

(for example, see Ref. 11). The matrix is the transition matrix given by Eq. (28) in the text, and $Q(\tau)$ is the covariance expectation of the plant noise,

i. e.,

$$E [\bar{v}(t) \bar{v}(\tau)] = Q(t) \delta(t-\tau) \quad (C2)$$

where $\bar{v}(t)$ is the plant noise vector in the canonical equation

$$\frac{d\bar{x}(t)}{dt} = F(t) \bar{x}(t) + \bar{v}(t) \quad (C3)$$

When random gyro drift is the only plant noise

$$\bar{v}(t) = \begin{bmatrix} v_1(t) \\ v_2(t) \\ v_3(t) \\ 0 \\ 0 \\ 0 \\ 0 \end{bmatrix} \quad (C4)$$

where $v_1(t)$, $v_2(t)$, and $v_3(t)$ are the expected random drift components along the orthogonal axes, and are assumed to be white noise over the spectrum of interest. Substituting this in Eq. (C2) yields

$$Q(t) = \begin{bmatrix} v_1^2 & 0 & 0 & 0 & 0 & 0 \\ 0 & v_2^2 & 0 & 0 & 0 & 0 \\ 0 & 0 & v_3^2 & 0 & 0 & 0 \\ 0 & 0 & 0 & 0 & 0 & 0 \\ 0 & 0 & 0 & 0 & 0 & 0 \\ 0 & 0 & 0 & 0 & 0 & 0 \end{bmatrix} \quad (C5)$$

In order to obtain a closed form solution for \bar{x} from

$$\dot{\bar{x}}(t, \tau) = [F(t)] \bar{x}(t, \tau) \quad (C6)$$

$F(t)$ must be describable by a continuous analytic function. If it is assumed that $\psi = \phi = c$ and $q = \text{const.}$ in $F(t)$ [Eq. 29 of the text], then $\bar{x}(t, \tau)$ becomes

$$\bar{x}(t, \tau) = \begin{bmatrix} \cos qt & 0 & -\sin qt & \frac{1}{q} \sin qt & 0 & -\frac{1}{q}(1-\cos qt) \\ 0 & 1 & 0 & 0 & t & 0 \\ \sin qt & 0 & \cos qt & \frac{1}{q}(1-\cos qt) & 0 & \frac{1}{q}(\sin qt) \\ 0 & 0 & 0 & 1 & 0 & 0 \\ 0 & 0 & 0 & 0 & 1 & 0 \\ 0 & 0 & 0 & 0 & 0 & 1 \end{bmatrix} \quad (C7)$$

If it is further assumed that star transits occur frequently enough that $\cos qt \approx 1$ and

$\sin qt \approx qt$, then:

$$\bar{x}(t, \tau) = \begin{bmatrix} 1 & 0 & -qt & t & 0 & 0 \\ 0 & 1 & 0 & 0 & t & 0 \\ qt & 0 & 1 & 0 & 0 & t \\ 0 & 0 & 0 & 0 & 0 & 0 \\ 0 & 0 & 0 & 0 & 0 & 0 \\ 0 & 0 & 0 & 0 & 0 & 0 \end{bmatrix} \quad (C8)$$

Substitution of Eq. (C5) and (C8) into (C1) and integrating yields

$$U(t) = \begin{bmatrix} v_1^2 \Delta t_T & 0 & 0 & 0 & 0 & 0 \\ 0 & v_2^2 \Delta t_T & 0 & 0 & 0 & 0 \\ 0 & 0 & v_3^2 \Delta t_T & 0 & 0 & 0 \\ 0 & 0 & 0 & 0 & 0 & 0 \\ 0 & 0 & 0 & 0 & 0 & 0 \\ 0 & 0 & 0 & 0 & 0 & 0 \end{bmatrix} \quad (C9)$$

where $\Delta t_T = t - t_k$ and the assumptions have been made that:

$$v_i^2 \gg (v_1^2 - v_3^2) qt$$

and

$$v_i^2 \gg v_i^2 q^2 t^2$$

REFERENCES

1. W. R. Davis and J. A. Miller, "SPARS - A Completely Strapdown Concept for Precise Determination of Satellite Vehicle Attitude," Presented to the Spacecraft Attitude Determination Symposium, The Aerospace Corporation, September 30 to October 2, 1969.
2. "(U) Space Precision Attitude Reference System," Vol. 1 Technical Proposal, (Confidential), LMSC 699615, 15 May 1967.
3. W. R. Davis et al., "(U) Space Precision Attitude Reference System (SPARS) Phase O Final Report," Vols. I and II (SECRET), LMSC B098019, SAMSO - TR - 68 - 219, April 1968.
4. R. T. Scott and J. E. Carroll, "Development and Test of Advanced Strapdown Components for SPARS," Presented to the Spacecraft Attitude Determination Symposium The Aerospace Corporation, September 30 to October 2, 1969.
5. John J. Sullivan, "A Solution of the Critical Computational Problems Associated with Strapdown Navigation Systems," AIAA/JACC

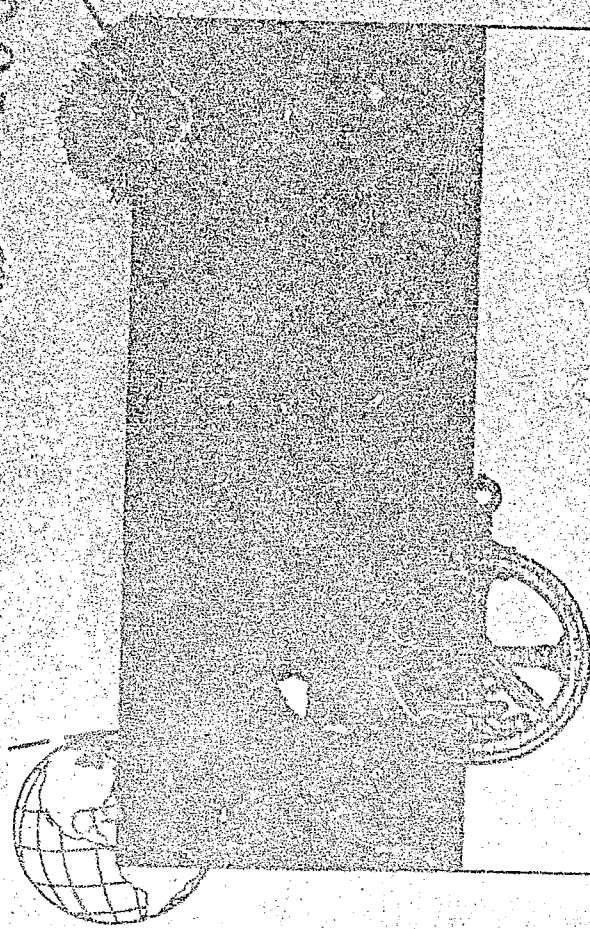
- Guidance and Control Conference, Seattle, Washington, August 15-17, 1966.
6. W. K. Clarkson, "Long Life Digital Attitude Control System - Estimate of Computational Requirements," Aerospace Report No. TR-1001 (2307)-13, Air Force Report No. SSD-TR-67-136, April, 1967.
 7. Dr. Joseph L. LeMay, "Theory and Applications of Linear Estimation Theory," Instrument Society of America Preprint 3.2-1-65, October 4-7, 1965.
 8. D. B. Jackson, "Applications of Nonlinear Estimation Theory to Spacecraft Attitude Determination Systems," Presented to the Spacecraft Attitude Determination Symposium, The Aerospace Corporation, September 30 to October 2, 1969.
 9. Smithsonian Astrophysical Observatory Star Catalog, Smithsonian Institute, Washington, D. C., 1966.
 10. V. Hvoschinsky and F. Y. Horiuchi, "Concepts and Mechanization for Evaluating PEPSY in the Laboratory and in Orbit," Presented to the Spacecraft Attitude Determination Symposium, The Aerospace Corporation, September 30 to October 2, 1969.
 11. A. E. Bryson and Y. C. Ho, Applied Optimal Control (Blaisdell Publishing Co., Waltham, Mass., 1969) Appendix A4.

AD704600

*PROCEEDINGS
OF THE
SYMPOSIUM ON
SPACECRAFT
ATTITUDE
DETERMINATION*

*September 30,
October 1-2, 1969*

VOLUME I
UNCLASSIFIED PAPERS



Cosponsored by AIR FORCE SYSTEMS COMMAND
Space and Missile Systems Organization
and THE AEROSPACE CORPORATION

Held at The Aerospace Corporation
2350 El Segundo Boulevard
El Segundo, California

69 OCT 31

Reproduced by the
CLEARINGHOUSE
for Federal Scientific & Technical
Information Springfield Va 22151

DDC
DECLASSIFIED
MAR 16 1975
REPRODUCTION
B

THIS DOCUMENT HAS BEEN APPROVED FOR PUBLIC
RELEASE AND SALE; ITS DISTRIBUTION IS UNLIMITED

424

Air Force Report No.
SAMSO-TR-69-417, Vol I

Aerospace Report No.
TR-6066(5306)-12, Vol I

PROCEEDINGS OF THE SYMPOSIUM ON
SPACECRAFT ATTITUDE DETERMINATION,
SEPTEMBER 30, OCTOBER 1-2, 1969

Volume I: Unclassified Papers

Cosponsored by
AIR FORCE SYSTEMS COMMAND
Space and Missile Systems Organization
and THE AEROSPACE CORPORATION

Held at
THE AEROSPACE CORPORATION
2350 El Segundo Boulevard
El Segundo, California

69 OCT 31


This document has been approved for public
release and sale; its distribution is unlimited

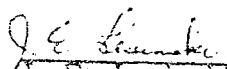
FOREWORD

These proceedings are published by The Aerospace Corporation, El Segundo, California, under Air Force Contract No. F04701-69-C-0066. Any other applicable contract number or company sponsorship is cited in a footnote on the first page of the individual paper.

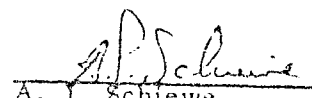
This document was submitted on 4 December 1969, for review and approval, to Captain D. Evans, SAMSO (SMTAE).


L. J. Henrikson
The Aerospace Corporation
Cochairman


D. Evans, Captain, USAF
SAMSO
Cochairman


J. E. Lesinski
The Aerospace Corporation
Cochairman

The views expressed in each paper are those of the author. Publication of this report does not constitute Air Force or Aerospace approval of the report's findings or conclusions. It is published only for the exchange and stimulation of ideas.


A. J. Schiewe
Director, Control and Sensor
Systems Subdivision
Electronics Division
Engineering Science Operations
The Aerospace Corporation


D. Evans, Captain, USAF
Project Officer

PREFACE

The Symposium on Spacecraft Attitude Determination was held at The Aerospace Corporation, El Segundo, California, on September 30 and October 1-2, 1969. It was cosponsored by the Air Force Systems Command, Space and Missile Systems Organization, and The Aerospace Corporation.

The symposium brought together 306 representatives from 44 industrial, governmental, and educational organizations concerned with spacecraft attitude determination.

The purpose of the symposium was in general to present a broad coverage of the spacecraft attitude determination problem and in particular to review the advances in sensing and data processing techniques related to spacecraft attitude determination, to assess current capabilities, and to provide an exchange of ideas among people who have an active interest in the field. The sponsors hope that the symposium has stimulated new ideas and will lead to the advancement of spacecraft attitude determination potentials.

Symposium cochairmen were D. Evans, Captain, USAF, L. J. Henrikson, and J. E. Lesinski.